

Quantifying Uncertainties in CERES/MODIS Downwelling Radiation Fluxes in the Global Tropical Oceans

Venugopal Thandlam (✉ venux4@gmail.com)
Uppsala University

Research Article

Keywords: CERES, MODIS, downwelling shortwave radiation, downwelling longwave radiation, global tropical oceans, GTMBA.

Posted Date: March 21st, 2022

DOI: <https://doi.org/10.21203/rs.3.rs-1458712/v1>

License:  This work is licensed under a Creative Commons Attribution 4.0 International License.
[Read Full License](#)

Abstract

The Clouds and the Earth's Radiant Energy System (CERES) program using the Moderate Resolution Imaging Spectroradiometer (MODIS) (CM) has been updated with a launch of new satellites and made newly upgraded radiation data available. Here we study the spatial and temporal variability of daily averaged synoptic 1-degree (SYN1deg) CM version 3 (CMv3) (old) and version 4 (CMv4) (new) downwelling shortwave (Q_S) and longwave radiation (Q_L) data in the global tropical oceans spanning 30°S-30°N available during 2000–2017. Daily in situ data from Global Tropical Moored Buoy Array (GT MBA) has been used to validate the CM data during 2000–2015. Both Q_S and Q_L in CMv4 show significant enhancements with improved bias, root-mean-square error, and standard deviations (standard deviation) compared to CMv3. Furthermore, long term trend analysis shows that Q_S has been increasing in the southern hemisphere with 1 Wm^{-2} per annum. In contrast, the northern hemisphere shows an annual decreasing trend of -0.7 Wm^{-2} . Both Q_S and Q_L shows similar spatial trend pattern. However, Q_L spatial patterns in CMv3 and CMv4 differ largely with an opposite trend (0.5 Wm^{-2}) in the Indian Ocean, Indo-Pacific warm pool region and southern hemisphere. These annual trends in Q_S and Q_L could cause Sea Surface Temperature (SST) to change in the tropical oceans with a magnitude of -0.2 to 0.3°C per annum. These results stress the importance of accurate radiative flux data, and CMv4 data can be used as a better alternative radiation data to force standalone ocean models than reanalysis products. They may also be helpful to produce hybrid data by correcting reanalysis or other model-simulated data.

Plain Language Summary

Downwelling radiation plays a key role in modulating global weather and climate patterns. This work studies the variability of different versions of downwelling radiation data in the global tropical oceans available from the Clouds and the Earth's Radiant Energy System (CERES) program. We also found uncertainties in these datasets using the Global Tropical Moored Buoy Array (GT MBA) observations. Both downwelling shortwave and longwave data in the global tropical ocean show improvements in CMv4 compared to CMv3. The annual climatological difference between CMv3 (old version) and CMv4 (new version) (CMv3-CMv4) shows large positive values of downwelling shortwave radiation in the tropical Pacific and large positive values of downwelling longwave radiation in the Indian Ocean. Though the new version was improved significantly, some uncertainties still exist in the data. Thus, the recommended is to consider these errors while using the data to study the various ocean and atmospheric processes.

Key Points

CERES/MODIS downwelling radiation fluxes have been validated with daily in situ data from the Global Tropical Moored Buoy Array during 2000-2015.

Downwelling shortwave radiation has increased in the southern hemisphere with $1 \text{ Wm}^{-2}/\text{year}$ and decreased in the northern hemisphere with $-0.7 \text{ Wm}^{-2}/\text{year}$.

Annual trends in downwelling radiation changes bring the -0.2 to 0.3° C per annum change in Sea Surface Temperature in the tropical oceans.

1. Introduction

The climate and weather forecasting model's performance depends on the availability of high-resolution accurate surface radiation datasets and their assimilation into the climate and weather forecasting models (Rahaman et al., 2019). The atmosphere and ocean interact mainly through mass, momentum, and heat fluxes at the ocean-atmosphere interface. The heat fluxes modulate the intraseasonal oscillations in the tropical oceans (Vialard et al., 2008; Sobel et al., 2008; Jayakumar et al., 2011). Shortwave radiation and latent heat flux are the principal contributors to heat flux variation in the tropics (Koberle et al. 1994). Tropical oceans receive the largest solar irradiance in the form of shortwave radiation. The excess heat over the tropical ocean balances through turbulent mixing, longwave radiation, and transport to the higher latitudes through ocean circulation for more extended periods (Trenberth et al. 2004). On weekly time scales, tropical and extra-tropical cyclones make up the most prominent energy transfer from the ocean to the atmosphere through the release of latent heat (Ma et al., 2015). Heat fluxes also influence the large-scale tropical coupled processes like El Niño Southern Oscillation (ENSO), Indian Ocean Dipole (IOD), Atlantic Meridional Mode (AMM) (Xie and Philander 1994; Wang et al. 1999; Murtugudde et al. 2001; Vialard et al. 2001; Hendon 2003; Vimont and Kossin 2007). Ocean General Circulation Models (OGCMs) use the near-surface atmospheric state to parameterize the heat and momentum flux (Large et al., 2009).

Similarly, uncertainties in turbulent and radiative heat fluxes could affect the heat balance in the boundary conditions prescribed in the OGCMs (Venugopal et al. 2016, Thandlam and Rahaman, 2019). These limitations in the forcing fields are partially responsible for the OGCMs to make unrealistic simulations of intra-seasonal, seasonal, inter-annual variability, and climatic features (McWilliams et al. 1996). Hence, accurate near-surface atmospheric fields are essential for realistic simulations in a forced ocean model.

The sum of net radiative flux and turbulent flux adds up to net air-sea flux at the sea surface (Fairall et al. 1996; Curry et al. 2004; Pinker et al. 2014). Longwave and shortwave radiation are the two components of radiative flux. The downwelling fluxes of shortwave (Q_S) and longwave radiation (Q_L), together with other meteorological variables and initial ocean state, force the OGCMs (Ocean General Circulation Models), and the ocean model simulation accuracy depends to a large extent on the accuracy of these downwelling radiative fluxes. At present, the ocean modeling community uses Common Reference Ocean-Ice Experiments (CORE-II) and JRA-do datasets as the prime source to run the global ocean and sea-ice model (Large et al. 2004, 2009; Tsujino et al. 2018; Kobayashi. et al. 2015). National Centre for Environmental Prediction (NCEP2) data released corrected data as CORE-II (Kanamitsu et al. 2002), and improved JRA reanalysis is called JRA-do. However, CORE-II uses the radiation data obtained from the International Satellite Cloud Climatology Project (ISCCP) (Zhang et al. 2004), available only until 2009. Hence, CORE-II forcing fields are not available beyond 2009. Therefore, climate forecasting system

reanalysis (CFSR, CFSv2) (Saha et al. 2010, 2014) replaced the NCEP2 data. Although other radiation data sets have taken over the ISCCP after 2009, still there are gaps in this area.

Ramesh et al. (2017) used satellite data (MODIS) as the reference to evaluate the radiative fluxes from Ocean Moored Network for the Northern Indian Ocean (OMNI). Rahaman et al. (2013) have evaluated the near-surface air temperature and humidity from CORE-II, Objectively Analysed Air-Sea Fluxes (OAFUX), and Tropical Flux (TropFlux) to find a better dataset to use in the model forcing. Evaluation of the surface radiation fluxes with buoy observations in the Pacific Ocean during 2000-2012 concluded that satellite data match well with the in-situ observations, followed by reanalysis and model data (Pinker et al. 2017a, 2017b, 2018). Trolliet et al. (2018) compared the irradiance data from MERRA-2 and ERA-5 and three other satellite-derived data sets: HelioClim 3v5, SARA 2, and CAMS with five buoys in the Atlantic for the period 2012-2013. At the ocean-atmosphere interface in the Atlantic, heat budgets derived from satellites and blended products were compared with in situ observations during 2003-2005 (Pinker et al. 2014). While the performances are similar between the three satellite-derived data sets, present existing reanalysis data have significant biases, errors, and poor correlation coefficient (CC) values compared with independent in situ observations. In addition, the Earth's radiation balance from satellite observations has a significant bias over the ocean than their better agreement over the land (Ma et al., 2012). These differences are due to frequent changes in satellite observing systems, degradation of sensors, restricted spectral intervals and viewing geometry of sensors, and changes in the quality of atmospheric inputs that drive the inference schemes.

1.1 Global Tropical Moored Buoy Array

Moored buoy observing systems in all three tropical oceans called Global Tropical Moored Buoy Array (GT MBA). This program is a multinational effort to get surface meteorological and subsurface oceanic near-real-time data for research and applications. It has three components, namely Tropical Atmosphere Ocean/Triangle Trans-Ocean Buoy Network (TAO/TRITON) in the tropical Pacific (McPhaden et al. 1998), Pilot Research Moored Array in the Tropical Atlantic (PIRATA) in the tropical Atlantic (Bourlès et al. 2008) and Research Moored Array for African-Asian-Australian Monsoon Analysis and Prediction (RAMA) in the tropical Indian Ocean (McPhaden et al. 2009). GT MBA (RAMA) program in the Indian Ocean is relatively new, as this program was first started in the Pacific and later followed by the Atlantic. The GT MBA data undergo rigorous three-stage quality control (daily, weekly, and monthly) procedures to ensure high accuracy standards before delivering to users (Freitag et al. 1999, 2001; Payne et al. 2002; Medovaya et al. 2002; Lake et al. 2003).

The uncertainty in Q_s in the GT MBA data is 2% due to drift criteria and reported monthly mean accumulation biases due to high-dust accumulation is as large as -200 Wm^{-2} in the Atlantic. Similarly, record-length mean biases in the Q_s from the moorings in the Atlantic (PIRATA) can be -10 Wm^{-2} , potentially leading to significant negative Q_s biases (Foltz et al., 2013). Thandlam and Rahaman (2019) and the references detailed the GT MBA project. Among 27 mooring sites in the Indian Ocean, daily averaged (0000 UTC to 2300 UTC) Q_L data is available only at 0°N , 80.5°E ; 15°N , 90°E and 8°S , 67°E

(three locations); while daily averaged Q_S data (0000 UTC to 2300 UTC) are available at 19 sites during the study period. Among the 7 stations delivering Q_L in the Atlantic Ocean, only 4 have consistent data, and Q_S was available over 17 out of 21 locations during the study period. The Pacific Ocean has more moorings with better data availability than other oceans. We use the Q_L data delivered from 11 moorings and Q_S data obtained from 32 out of 34 sites in the Pacific Ocean. We used all available mooring locations for Q_S and Q_L in the tropical oceans during 2000-2015. Thus, more Q_S observations with widespread are available than less and sparsely distributed Q_L observations in the tropical oceans. However, many buoy locations have data gaps, and few stations exist where only Q_S or Q_L are available. Therefore, the data availability period of all mooring sites is not the same. Data gaps and the spuriousness of mooring data are paid attention to while validating satellite data with GTMBA data. Supplementary figure 1 shows the present status of GTMBA and the location of buoys.

1.2 Clouds and Earth's Radiant Energy System

The Earth Radiation Budget Experiment (ERBE) (Barkstrom et al. 1986; Barkstrom et al. 1989) provided important information about energetics and effects of clouds in modulating the energy balance (Ramanathan et al. 1989; Harrison et al. 1990). The CM project started in 1997 (PFM instrument) is conceived as a successor to ERBE to compile a data record for the investigation of interannual variations of climate (Harrison et al. 1990; Wielicki et al. 1998; Kato et al. 2013) and provides an alternative for the radiative flux components available since 2000 to till date (Barkstrom et al. 1989; Wielicki et al. 1998; Kato et al. 2013). The CM project produces a long-term, integrated global climate data record for detecting decadal changes in the Earth's radiation budget from the surface to the top-of-atmosphere. Thus, the CM program supports climate model evaluation and improvement through model-observation inter-comparisons. CM is the only project to produce global climate data records of Earth's radiation budget using polar-orbiting and geostationary satellites accounting for variations in radiation at hourly, daily, and monthly timescales and at spatial scales ranging from 20 km to 1° .

The CM program focused on measuring outgoing longwave radiation (OLR) radiances to an accuracy of 1% and reflected solar radiances to 2%. In total, there are 7 instruments launched, with the latest one (FM6) launched in 2017 on the National Oceanic and Atmospheric Administration's (NOAA) Joint Polar Satellite System 1 (JPSS-1). The release of the instrument and ERBE-like data from FM6 occurred in June 2018. These instruments and platforms used to collect this data include Imaging Radiometers on Geostationary Satellites platform; CERES Flight Model 1 (FM1), CERES FM2, CERES Scanner, and Moderate-Resolution Imaging Spectroradiometer (MODIS) on Terra; and CERES FM3, CERES FM4, CERES Scanner, and MODIS on Aqua. CM estimates of incident solar radiation agree better with surface measurements at monthly rather than at daily timescales. These estimates can also capture the seasonal variation of incident solar radiation very well (Wielicki et al. 1996). Rutan et al. (2015) compared CM surface radiation flux data at 85 globally distributed land (37) and ocean buoy (48) surface observations as well as several other publicly available products on global surface radiation flux data. The downward fluxes from SYN1deg have a monthly bias (standard deviation) of 3.0 Wm^{-2} (5.7%) for Q_S and -4.0 Wm^{-2}

(2.9%) for Q_L compared to surface observations. Inclusion of the diurnal cycle of cloud changes minimized the standard deviation between surface Q_S flux calculations and observations at the 3-hourly time scale. Kato et al. (2013) estimated the bias (RMSE) between computed and observed monthly mean irradiances calculated with ten years of CM data as 4.7 (13.3) Wm^{-2} for Q_S and -2.5 (7.1) Wm^{-2} for Q_L over global oceans. Barkstrom (1999) and Smith et al. (2011) presented complete technical details and status of CM.

Past studies evaluated radiative fluxes from different satellites with observations over the land and the ocean (Pinker 2009, 2014, 2017a, 2017b and 2018). Nevertheless, all these studies either have a single downwelling radiation parameter or focus on a narrow region for a brief period. Venugopal et al. (2016) and Thandlam and Rahaman (2019) performed a similar analysis in the global tropical oceans, with a subset of Moderate Resolution Imaging Spectrometer (MODIS) from the Clouds and Earth's Radiant Energy System (CERES), hereafter CM, version 3 datasets during 2000-2009. In the present work, we evaluate both the components of downwelling radiation (Q_S and Q_L) from CM version 3 (CMv3) and CM version 4 (CMv4) for a longer period (2000-2017). As per our knowledge, there is no study focused on validating near-surface Q_S and Q_L from updated CMv4 data in the tropical oceans with in-situ observations for a longer period.

Hence, this study aims to undertake a comparison of the Q_S and Q_L from the regularly updated downwelling radiation from satellite data over the tropical oceans with in-situ observations, to assess whether CMv4 data can be complementary to the reanalysis data to force the OGCMs and can be used to evaluate climate models. Evaluating both versions with independent in situ observations over the global tropical oceans could give a glimpse of their performance and help to choose them in developing a hybrid/blended forcing data including other atmospheric and ocean variables. We also study the spatial variability of CM (Q_S and Q_L) available during 2000-2017. This paper is organized as follows. Section 2 describes the various datasets used in this study. Section 3 discussed the evaluation of satellite data with in-situ observations. Section 4 focuses on spatial variability and quantifies the annual SST change due to annual trends in Q_S and Q_L from CMv4. We illustrated the details and results of the validation process with reference data from the Global Tropical Moored Buoy Array (GT MBA) (McPhaden et al., 2010). The main conclusions and summary are in section 4.

2. Data And Methodology

We use GT MBA mooring radiation data (McPhaden et al. 2010) to evaluate Q_S and Q_L fluxes from CM available in real-time during 2000–2015. We compare these products with GT MBA collocated and concurrent data sets with nearest grid-point data. Trolliet et al. (2018) show that comparing point location with gridded data is valid over the tropical Atlantic Ocean since no strong systematic gradient in irradiance was present over a short distance in the tropical oceans. The mean, standard deviation (standard deviation), and root-mean-square error (RMSE) are computed using equations (1), (2), and (3) from Thandlam and Rahaman (2019).

Multiple data collection systems provide data from the Tropical Moored Buoy Array. The older "Next Generation ATLAS" systems have been replaced in TAO by National Data Buoy Center (NDBC) TAO Refresh system and are in the process of being replaced by Pacific Marine Environmental Laboratory (PMEL) recently developed "T-Flex" systems in PIRATA and RAMA. Pyranometer is the sensor used to measure the downwelling radiation fluxes with resolution 0.4 Wm^{-2} , range $0\text{-}1600 \text{ Wm}^{-2}$, and accuracy $\pm 2\%$ (Cronin et al., 1997; Foltz et al., 2013). The downwelling radiation data is sampled and stored at 1 min interval with a sampling rate of 1 Hz (Mangum et al., 1995). Hourly mean and standard deviation of data are transmitted in real-time through Global Telecommunications System (GTS). We used all-weather daily averaged (0000 UTC to 2300 UTC) GTMBA data obtained from the GTMBA data delivery platform to compensate with the daily averaged CM data. Though the real-time data have high frequency with cloud variability on a buoy compared to time-averaged values, unavailability of the high-frequency data over a few time steps in each day could lead to bias in the data. (Table 1 shows the details of the GTMBA data used in the present study.

Similarly, Fig. 1 shows the frequency distribution of GTMBA data in the tropical oceans during 2000–2015. Except in the higher range ($300\text{--}350 \text{ Wm}^{-2}$), the number of shortwave observations in the Indian Ocean and Atlantic shows a large difference with those in the Pacific (Fig. 1a). Similarly, the Atlantic receives no longwave observation beyond 450 Wm^{-2} (Fig. 1b).

In the present study, we have used observed geostationary enhanced, temporally interpolated surface radiative fluxes for all-sky conditions CMv3 and CMv4 (CM version 4) (Loeb et al., 2018) data of Q_S and Q_L . Data are obtained from seven CERES instruments (<https://ceres.larc.nasa.gov/instruments/>) on five satellites launched (TRMM, Terra, Aqua, S-NPP, NOAA-20). The Langley Fu-Liou radiative transfer model produces the top of the atmosphere fluxes. Though CM Synoptic (SYN1deg) products (CMv3 and CMv4) provides hourly data (also have a temporal resolution of 3-hourly, daily, monthly hourly, and monthly), we use climate-quality global daily (temporarily averaged), $1^\circ \times 1^\circ$ (spatially) gridded surface radiant fluxes (Q_S and Q_L from CMv3 and CMv4) available during 2000–2017 (Venugopal et al. 2016; Doelling et al., 2013, 2016). We use the daily averaged CM data to evaluate daily in-situ observations from the GTMBA. To have a glimpse of spatial patterns of the data, Figure S2a shows the 3-hourly Q_S data from CMv3 on 28th February 2017, and Figure S2b shows the global daily mean of computed Q_S from 3 hourly data. Rutan et al. (2015) detailed the product computation, methods, and validation of CM. Finally, we have used EN4-Hadley interpolated monthly mean temperature profiles with 1° spatial resolution to compute mixed layer depths (MLD) climatology in the global tropical oceans to estimate the annual change in SST due to the annual trend in Q_S and Q_L from CMv4. These datasets are obtained from Met Office Hadley Centre observations datasets during 1993–2017 (Good et al., 2013). These temperature profiles are at 42 depth levels from 5 m to 5250 m.

3. Results And Discussions

3.1 The Indian Ocean

Figure 2 shows the frequency distribution of downwelling shortwave and longwave radiation data in the Indian Ocean. This figure used all the available concurrent and collocated data from the RAMA buoy locations (19). This number turns out to be 42412 and the same for all (RAMA, CMv3 and CMv4). It can be seen that most of the Q_S values lie in the 200-300 Wm^{-2} range. Satellite-derived products underestimate the lower ($< 150 Wm^{-2}$) and higher ranged values ($>300 Wm^{-2}$). Slightly better agreement in CMv4 Q_S product is seen concerning observations in the lower ($< 150 Wm^{-2}$) and higher ($>300 Wm^{-2}$) ranges as compared to CMv3. The mismatch in the satellite-derived products with the lower and higher limits of Q_S observations in the Indian Ocean could be due to the retrieval error or may have arisen due to the large intra-seasonal, seasonal, and inter-annual variability over this region. Both satellite-derived products overestimated the Q_S in the 150-250 Wm^{-2} range compared to observation (Figure 2a). The maximum number of observations (~ 14000) falls in the 250-300 Wm^{-2} range, and both the satellite-derived products are very near to this observed value. On the other hand, most observations and satellite Q_L data lie in the range of 350-450 Wm^{-2} . Q_L data retrieved from the CM shows a good fit with observations in all ranges (Figure 2b). Thus, both versions of CM are coherent in sensing the downwelling longwave data in the Indian Ocean. Figures 3 and 4 show the temporal variability of Q_S and Q_L , respectively, over selected locations with reasonably continuous data availability. Each sub-panel also gives the mean and standard deviations (standard deviation) values of observation and satellite products. Both CMv3 (red) and CMv4 (blue) show similar temporal variability with observations (black). While Q_S from observations and both versions of CM data in the equatorial region show the absence of prominent seasonal variability (Figure 3b-3d), but the seasonal changes are significant in the northern Bay of Bengal (Figure 3a) and the thermocline ridge region over the south-western Indian Ocean (Figure 3e). The observed Q_S over the northern Bay of Bengal (Figure 3a) peaks in the spring due to clear sky conditions with the highest solar insolation (Weller et al., 2016) and shows low values in the summer and winter months to cloudy conditions and precipitation during summer and winter monsoon. Low Q_S values below 150 Wm^{-2} over different stations could be due to the weekly resolved radiation transfer algorithms during the presence of deep convective clouds and aerosol optical depth (Koren et al., 2010). The satellite-derived Q_S products can capture the observed temporal variations over all the RAMA buoy locations (Fig-3a-e). The statistical values show that the CMv4 product performs slightly better than CMv3 in terms of mean and standard deviation compared with observed values. Hence, the CMv4 product could be a better option to study the Indian Ocean radiative flux variability studies and validation of other products.

Contrary to Q_S , Q_L shows large values over the northern Bay of Bengal during the summer and winter months due to cloudy conditions and low values during spring due to relatively clear sky conditions (Figure 4a). Though the CMv4 Q_L mean (411.5 Wm^{-2}) is close to the observed mean, the CMv3 data show a better standard deviation (26.3 Wm^{-2}) in the northern Bay of Bengal. On the other hand, Q_L from CMv4 shows better agreement with observations both in standard deviation and mean (Figure 4a). Following the Q_S , Q_L also shows no seasonal, and intra-seasonal variability over the equator, and values lie above

400 Wm⁻²; thus, this region receives large Q_L irrespective of the season. The location of this station is in the eastern equatorial Indian Ocean, and these high values could be corresponding to the persistent convective clouds due to the presence of ITCZ throughout the year (Deckker 2016). However, there is no significant improvement in the CC between observations and Q_L from CMv4 (CC=0.89) compared to CMv3 (CC=0.87) in the Indian Ocean (Figure 5). It could be due to Q_L being underestimated by CMv4 and CMv3 in the higher range (>450 Wm⁻²), as shown in Figure 5a and Figure 5b, respectively.

Table 2 shows the statistics of both Q_S and Q_L from all stations in the Indian Ocean compared with observations during 2000-2015. While both CMv3 and CMv4 overestimate the Qs with the positive bias of 1.43 Wm⁻² in CMv4 and 4.5 Wm⁻² in CMv3. It is worth mentioning that this daily mean bias is much less than the earlier reported monthly biases compared with similar buoy observations (Rutan et al., 2015; Kato et al., 2013). The RMSE in CMv4 (27.34 Wm⁻²) is significantly lower than CMv3 (41.33 Wm⁻²). However, both the satellite products cannot capture the variability in standard deviation, yet CMv4 is near observed values than CMv3. The Q_S in CMv4 shows better CC (0.92) than CMv3 (0.80).

Q_L underestimated the observations with the negative bias of 6.95 Wm⁻² and 3.15 Wm⁻² in CMv3 and CMv4, respectively. Other statistical values also show improvement in CMv4 compared to CMv3 (Table 2).

3.2 Tropical Atlantic Ocean

Though the tropical Atlantic is the smallest in the tropical oceans, the intraseasonal and interannual variability of downwelling radiation over this region is key to global climate processes. Among other atmosphere-ocean phenomena, the intertropical convergence zone (ITCZ) variability twice a year defines the evolution of synoptic-scale oscillations in the Atlantic. The fluctuations in downwelling radiation received due to variability in cloud cover control the intensity of Atlantic zonal mode and meridional modes in the tropical Atlantic (Murtugudde et al. 2001). Also, these synoptic oscillations induce changes in the global monsoon precipitation patterns and the poleward movement of heat and momentum (Sabeerali et al., 2019; Woollings et al., 2012). The frequency distribution of Q_S and Q_L in the Atlantic is shown in Figure 6. Unlike the data-scarce Indian Ocean, the number of observations is more in the Atlantic Ocean. Satellite-derived products underestimated the observed Q_S below 200 Wm⁻² and above 300 Wm⁻². The satellite products overestimate the observed values in the 200-300 Wm⁻² range. Both CMv3 and CMv4 show a similar distribution and have no significant QS improvement from the upgraded version (CMv4) in the Atlantic (Figure 6a). The discrepancies in the satellite estimations of shortwave radiation could be due to the ineffectiveness of radiative transfer models in estimating the Q_S during cloudiness and precipitation.

Nevertheless, Q_L in the CMv4 shows better agreement than the CMv3 (Figure 6b). Most of the observed values lie in the 350-450 Wm⁻² range, and both satellite products could be able to capture the observed distribution in this range, with CMv4 slightly better when compared with CMv3. However, downwelling fluxes are primarily a function of local cloud properties, the discrepancies between satellite products and

in situ measurements in the lower and higher range cloud are also due to errors in retrieving cloud optical thickness and surface albedo in the satellite data (Riihelä et al., 2017)

Furthermore, temporal variability of Q_S from PIRATA compared with CMv3 and CMv4 are shown in Figure 7. The prominent intra-seasonal oscillations in Q_S dominate the seasonal and interannual oscillations over the equator (Figure 7b). However, the seasonal cycle is more dominant off the equator than the intraseasonal oscillation (Figure 7a, c, d). The northward movement of ITCZ in boreal spring increases the cloud cover, leading to low Q_S over the equator. While CMv4 shows a better standard deviation (37.1 Wm^{-2}) with observations (44 Wm^{-2}), both versions of CM captured these oscillations. Seasonal and interannual oscillations of Q_S are dominant in the north and south of the equator (Figure 7a, 7c and 7d). However, Q_S in the North Atlantic shows low values in the winter and peaks in the boreal summer and vice versa in the southern Atlantic. Thus, the ITCZ movement plays a key role in modulating the intensity of Q_S in the Atlantic, and thus the SST, continental monsoon forcing, and air-sea interactions (Xie and Carton., 2004). The CMv4 shows an improved standard deviation than CMv3 compared with observations over all locations. This enhancement in the CMv4 is also reflected in the CC (0.89), which is low in the CMv3 (0.79) (supplementary figure S3b1, b2).

Similarly, Q_L from CMv4 is also controlled by the location of ITCZ and shows better agreement with standard deviation values nearing the observations over all locations. However, CC values (0.82) show no improvement in CMv4 compared to CMv3 (CC=0.82, Figure 9). Nevertheless, both products display a tight fit with the observations with less scattering in the higher range as noticed in the Indian Ocean. While Q_L in the equator and North Atlantic has seasonal and interannual variability (Figure 8a and 8b), south of the equator shows no such signal (Figure 8c). Substantial intra-seasonal variability dominates Q_L at 10°S instead. Q_L starts to peak in boreal spring at the equator, shows low summer values and is opposite in the north. At the same time, Q_L in the south Atlantic shows no such strong signal. Table 3 shows the detailed statistics of satellite data compared with observations over all locations in the Atlantic. Like the Indian Ocean, both Q_S in CMv4 (7.4 Wm^{-2}) and CMv3 (4.4 Wm^{-2}) overestimate the buoy observations in the Atlantic. RMSE in CMv4 (26.18 Wm^{-2}) is also lower than CMv3 (35.84 Wm^{-2}). Variability represented by standard deviation is also closer to observed values in CMv4 than CMv3. Q_L in CMv4 overestimated the observations with a positive bias while CMv3 underestimated. All other statistical values of Q_L in CMv4 also agree well with observations.

3.3 Tropical Pacific Ocean

The availability of in situ data in the tropical Pacific is more than that in the Atlantic and Indian Oceans. Figure 10 shows the frequency distribution of both Q_S and Q_L collocated with in situ observations for different ranges in the tropical Pacific. We used concurrent data; hence total numbers are the same for in-situ and satellite products. The Q_S shows a large range with a major distribution ranging from $50\text{-}350 \text{ Wm}^{-2}$. On the other hand, Q_L from both observations and CM show values between $300\text{-}400 \text{ Wm}^{-2}$. Like

the Indian Ocean, Q_s from CM significantly differ with observations in lower and higher ranges, while Q_L from CM shows no such difference with observations in the tropical Pacific.

Figure 11 shows the temporal variation of Q_s from both CMv3 (red) and CMv4 (blue) compared with TAO/TRITON (black) during 2000-2015 over the selected locations in the tropical Pacific Ocean. Gaps in the observations time series (black lines) are due to the unavailability of TRITON data during those periods. The satellite-derived products have captured the observed strong intra-seasonal variability of Q_s in the western tropical Pacific Ocean (Figure 11a, b: 170° W and 165° E). These two buoys are in the west Pacific warm pool region, and the ISO variability could be due to strong convection and large variability of the amount of cloud fraction over the warm-pool region (Wang and Mehta 2008). Thus, the Q_s over the eastern tropical Pacific vary between 150-350 Wm^{-2} . CMv4 agrees with TRITON data with better mean and standard deviation values than CMv3 over the eastern Pacific with strong seasonal variations. Particularly, both 110° W and 140° W stations persistently receive large Q_s above 200 Wm^{-2} . Also, the variability of Q_s over both western (165° E) and eastern (110° W) Pacific shows a strong ENSO impact. This can be seen in the drop of Q_s values. Q_s dropped below 200 Wm^{-2} for a brief period over these stations (Figure 11c and 11d) during ENSO events of 2002 and 2009-10 and could be associated with strong convection and cloud formation, which are opaque to the downwelling shortwave radiation (Li et al., 2017). Q_s from CMv4 shows better CC (0.90) with observations than CMv3 (0.79) (supplementary figure S3C). Also, low RMSE (28.91 Wm^{-2}) and bias (-0.67 Wm^{-2}) in CMv4 highlight its improved performance in the tropical Pacific as well (table 4).

Q_L from CMv4 in the tropical Pacific shows better performance than CMv3. However, marginal improvements were observed in parameters such as standard deviation, RMSE, and CC (Table 4). Satellite data did not capture higher observations and show large biases, as shown in Figure 13. Nevertheless, Q_L in CMv4 overestimated the observations with positive bias ($\sim 5 Wm^{-2}$), while CMv3 underestimated the TRITON data with negative bias (3.26 Wm^{-2}). All statistics of both Q_s and Q_L compared with TRITON data are shown in table 4. The time series of Q_L collocated with observations over various locations in the tropical Pacific during 2006-2015 is shown in Figure 12. Q_L shows no large seasonal variability; rather, intra-seasonal variability is embedded in the inter-annual variability at all locations. Both versions of satellite data could capture these variations at various locations in the tropical Pacific (Figure 12). Q_L over 170° W, 165° E, and 140° W show the impact of the strong negative phase of ENSO during 2010-2011, with values dropping below 400 Wm^{-2} due to the shift in the convection and clouds during this period.

4. Spatial Variability Of Downwelling Radiation

Spatial variability of both versions of CM is studied during 2000–2017 to compare and study the enhancements in the CMv4 with CMv3. Figure 14 shows the seasonal mean of Q_s from CMv3 (a-d) and CMv4 (e-h). Whilst both CMv4 and CMv3 show similar seasonal patterns, CMv4 shows lower mean values than CMv3 during all seasons. High Q_s in each hemisphere have a strong coupling with a shift in

the thermal equator. The northward shift in the ITCZ in spring caused Q_s to show large values in the northern hemisphere during MAM and JJA. While the ITCZ is in the south, the southern hemisphere receives large Q_s . Southcentral Indian Ocean, central Pacific, south-eastern Pacific, and south-western Atlantic receive high insolation stretching along 0-30°N during austral summer. Similarly, Q_s show high values in the northern hemisphere along 10-25°N during spring and summer. On the other hand, Q_s in different seasons show large spatial variability (standard deviation) over regions with low mean values (supplementary figure S4). Thus, the equatorial Indian Ocean, Bay of Bengal, south-eastern, and equatorial Pacific show large standard deviation ($\sim 60 \text{ Wm}^{-2}$) during spring, summer, and autumn. Contrary to Q_s , Q_L in CMv3 and CMv4 shows large values in the tropical Oceans between 10°S-10°N irrespective of the season (Fig. 15). These large values in the equatorial belt correspond to a large cloud due to high convection caused by the intense insolation (Hartmann et al., 2001). Mainly, Q_L is high over the Indo-Pacific warm pool region during all seasons. Q_L from both CMv3 and CMv4 in the north Indian Ocean shows large values in summer due to reflected longwave radiation from high cloud fraction during ISMR (JJA season) (Hazra et al. 2017). However, improvements in CMv4 lead to higher Q_L values ($> 420 \text{ Wm}^{-2}$) in the tropical oceans than those in CMv3. Thus, the difference in Q_L between both versions is around 20 Wm^{-2} in the tropical Oceans. This bias in two versions highlights the need to perform necessary corrections of the same order in the hybrid or reanalysis products developed, OGCMs forced and climate models (such as CMIP5 and CMIP6) evaluated using CMv3 data. However, there was no notable change in the spatial variability of Q_L in tropical Oceans both in CMv3 and CMv4, which lies around 5 Wm^{-2} (supplementary figure S5). However, a narrow stretch of tropical eastern Pacific, which is more prone to ENSO evolution and its annual variability, shows a standard deviation of 15 Wm^{-2} in both versions during all seasons.

Similarly, climatology of CMv3 and CMv4 show a significant difference between Q_s and Q_L spatially, as shown in Fig. 16. Q_s values in CMv4 show lower than CMv3 over central-east Pacific, Arabian Sea, and Indonesian Through Flow regions. As these regions are vital in controlling tropical weather patterns such as the evolution of ENSO, the advancement of the summer monsoon, and the development of IOD, these corrections in Q_s could enhance the study of these atmospheric-ocean phenomena in the tropical oceans. Similarly, Q_L in the CMv4 show slightly higher values than CMv3 over Indo-Pacific warm pool region and central Pacific. The climatological difference between CMv3 and CMv4 (CMv3-CMv4) for Q_s and Q_L is shown in Fig. 17. It can be seen there are sharp gradients in the central Pacific, central Atlantic, and the eastern Indian Ocean. These sharp gradients are due to the data product issue in CMv3. The CM products utilize 5 contiguous geostationary satellite imager hourly cloud retrievals to compute the surface fluxes. The boundaries between the satellite imagers are at 100 °E, 180 °E, 105 °W, 40 °W longitudes. The SYN1deg-hour, SYN1deg-day, and SYN1deg-month will have the same geostationary surface flux artifacts. Use of SYN1deg dataset at 3-hourly and daily time scales to find the bias between two versions has produced sharp gradients in the spatial patterns in Fig. 17. These discontinuities show up regardless of whether using hourly, daily, or monthly SYN1deg data in the different plots of CMv4 with CMv3. The

differences between the two products are not uniform. Q_s are overestimated in CMv4 than CMv3 over Pacific (except the south of central Pacific) and are around 10 Wm^{-2} (Fig. 17.)

Similarly, the northwest Atlantic and the north Indian Ocean also show overestimation in CMv4 (Fig. 17a) compared to CMv3. In general, CMv4 overestimates CMv3 throughout the global tropics. The spatial annual climatological difference for Q_L between both versions shows a mirrored pattern of Q_s with high in southern parts of the tropical oceans and low in the north. While the Pacific's difference lies at -10 Wm^{-2} , parts of western and southern Indian Ocean, south of central Pacific, off Chile and African coasts show the least difference between the two products (Fig. 17b).

We have done a long-term linear trend analysis to see whether any secular changes are reflected in the downwelling radiation data in the present global warming scenario. Figure 18 shows the annual trend of both Q_s and Q_L in the global tropical oceans from CMv3 and CMv4 during 2001–2017. Q_s from both versions of CM show a similar annual trend in the tropical oceans, with an annual increase of 1 Wm^{-2} in the southern hemisphere and a mean annual decrease of -0.7 Wm^{-2} in the northern hemisphere. However, CMv3 shows a larger negative trend (Fig. 18a) in the northern Pacific and Atlantic; and a positive trend in the southern Pacific and Atlantic than the Q_s trend in CMv4. On the other hand, parts of the eastern Pacific in both southern and northern hemispheres, including the southern Indian Ocean, show a large increase in Q_s in the CMv4 (Fig. 18b).

Similarly, the Q_s trend in the central tropical Pacific shows a lower magnitude in CMv4 than in CMv3. Improved Q_s in the CMv4 over the central Pacific and Indo-Pacific warm pool region may help understand air-sea interactions, walker circulation changes, and deep convection in tropical oceans. A major part of these positive and negative trends in Q_s in both CMv3 and CMv4 are significant at 95%, except in the central Atlantic and the north Indian Ocean in both versions. On the other hand, Q_L shows no such significant annual trends (Fig. 19a and 19b) except in a patch north of south America which shows a positive trend in CMv3. This highlights the strong annual changes in the Q_s than in Q_L in the global tropical oceans. However, Q_L over the south-eastern Atlantic shows an annual trend at 90% significance (Figure not shown). However, CMv4 shows no such prominent increasing trend of Q_L . Parts of central and north-eastern Pacific, southern Indian Ocean, and the south and the north Atlantic show a positive trend of mean Q_L at 0.3 Wm^{-2} (Fig. 19b). The annual trends computed using selected GTMBA stations for Q_s and Q_L over three tropical oceans are in coherence with the annual trends in the satellite products in the study period (Table 5). Though these stations are selected based on data availability, sparseness/discontinuous observations may lead to discrepancies in observed trends compared to trends in satellite data. Thus, improved and accurate downwelling radiation data over these regions as input to forcing the GCMs could reduce errors in the SST, mixed layer depths, and enhance the understanding of phenomena such as evolutions of ENSO and IOD, etc. and their teleconnections in the tropical oceans.

4. 1 Annual change in SST associated with the annual trend in Q_s and Q_L in CMv4:

SST anomalies play an important role in the upper ocean, lower atmospheric variability, and predictability (Venugopal et al., 2018; Thandlam et al., 2020; Kang et al., 2002). SST anomalies can also induce anomalous convection through surface evaporation and low-level moisture convergence (Kirtman and Vecchi, 2011). The anomalous atmospheric convection through cloud radiation, wind-evaporation, wind-induced oceanic mixing, and upwelling causes the SST to change. These atmospheric feedbacks can be detected in the SST tendency. The processes responsible for SST tendency differ from region to region over the tropical oceans. Also, errors in advection and heat flux over the tropical ocean are mainly responsible for the distortion of seasonal SST change in the coupled models (Chowdhury et al., 2015). Thus, it is essential to evaluate the role of different fluxes on SST and mixed layers. This study estimated the changes in mixed layer temperature due to the annual trend in Q_S and Q_L from CMv4. The mixed layer temperature or SST tendency equation is given as

$$\frac{\partial T_m}{\partial t} = \frac{Q_0 - Q_p}{\rho C_p H_m} + \frac{W_e (T_m - T_b)}{H_m} - U \cdot \nabla T_m - K_z + \frac{\partial^2 T_m}{\partial z^2} + R_s$$

1

where T_m denotes mixed layer temperature. K_z is the coefficient of vertical diffusion of heat ($0.1 \times 10^{-4} \text{ m}^2 \text{ s}^{-1}$). R_s is the residual term. W_e is the entrainment rate (ms^{-1}), and T_b is the temperature at the bottom of mixed layer. $\partial T_m / \partial t$ is the rate of change of T_m , ρ is seawater density (1024 kgm^{-3}), C_p is heat capacity of seawater ($3993 \text{ Jkg}^{-1} \text{ }^\circ\text{C}^{-1}$), and H_m is mixed layer depth. Q_0 is the net surface heat flux (Wm^{-2}), and Q_p is the shortwave radiation (Wm^{-2}) penetrating below the mixed layer (Du et al., 2005; Qiu 2003; Qu 2003). If heat fluxes are solely responsible for the SST change, then only the first term in the above equation is dominant, and all other terms can be neglected. We assume this approximation to show the maximum possible annual change in SST tendency due to the Q_S and Q_L annual trends. We also assume that the trend (annual change) is associated with corresponding Q_S and Q_L as net radiative heat flux, i.e. ($Q_0 - Q_p$) in the above equation. The MLD climatology was computed using Hadley monthly vertical temperature profiles data during 1993–2017, i.e., using 25 years of data (Good et al., 2013). A reference depth of 10 m, including temperature gradient criteria $\Delta T = 0.8 \text{ }^\circ\text{C}$, is used to compute the MLD from temperature profiles (Kara et al., 2000). The climatology of MLD computed is shown in Supplementary Figure S6. We used the same duration, i.e., 2000–2017, to prepare the climatology. We saw no difference in the SST change even if we used climatology made for a longer period (1993–2017). The Pacific and Atlantic show large MLDs ranging from 70 m to 100 m and are along the path of mean wind directions. The Indian Ocean shows relatively lower MLD with a maximum of 60 m. The maximum annual change in SST caused by the Q_S and Q_L annual trend in the global oceans is shown in Fig. 20. Positive Q_S trend in CMv4 causing southern hemispheric SSTs, particularly over the southern Indian Ocean, and south-eastern Pacific, to increase between $0.1\text{-}0.3^\circ\text{C}$ annually. Nevertheless, negative trends in Q_S over the northern hemisphere show no such large negative trends in SSTs (Fig. 20a). On the other hand, though Q_L annual positive trends show an increase in annual SST trends in the tropical oceans (Fig. 20b), these low

magnitude values (-0.1 to 0.1oC) could be less significant than low significant Q_L trends in Fig. 19a and 19b.

Conclusions

This study evaluated satellite-derived downwelling radiation data from two versions of CM in the global tropical oceans using the in-situ observations from the GTMBA program. Both radiative and turbulent heat fluxes are vital to understanding the air-sea interaction, global circulation patterns and heat and momentum exchange between the Atmosphere and Oceans. Notably, a large bias in radiation fluxes could induce bias in the SST, upper ocean heat content and variability in the global oceans (Thandlam and Rahaman 2019; Venugopal et al., 2016). These biases in the upper ocean could further lead to discrepancies in weather forecasting, studying upper ocean variability and understanding air-sea interactions (Venugopal et al., 2018; Thandlam et al., 2020; Ali et al., 2015). Similarly, accurate radiative fluxes in the analysis and numerical models could potentially lead to a better understanding of air-sea coupled processes such as ENSO, IOD, and MJO etc., in the tropical oceans and convection over time the warm ocean surfaces and their teleconnections. This could further greatly enhance weather forecasting and climate prediction (Venugopal et al., 2018).

In-situ data from GTMBA used in this study during 2000–2015 to evaluate the CM performance has more data points in the Pacific, followed by the Atlantic and the Indian Ocean. Both Q_S and Q_L from CMv4 show improvements compared to CMv3, but the performance of CMv4 is not homogeneous in the tropical oceans. Improvement in Q_S is robust in all three basins, but improvement in Q_L from CMv4 in the tropical Indian Ocean and tropical Pacific show slight improvements from CMv3. On the other hand, both in CC and RMSE of Q_L from CMv4 show a significant improvement in the Pacific compared to CMv3. However, Q_S in the CMv4 has been significantly enhanced over major parts of the tropical oceans. Improved satellite sensors, data retrieval techniques, radiative transfer algorithms and data processing techniques could have potentially contributed to the enhancements in the Q_S data in CMv4 over the tropical oceans. The magnitude and spatial patterns of both Q_L and Q_S from CMv3 and CMv4 are strongly coupled with ITCZ and the movement of the thermal equator during all seasons. Though both Q_S and Q_L show similar seasonal mean and variability (standard deviation) patterns, seasonal mean and standard deviation of Q_S from CMv3 are higher than CMv4 and seasonal mean and standard deviation of Q_L in CMv3 are lower than CMv4. However, persistent convection and large cloud fraction over major tropical oceans cause Q_L to be high during all seasons. Annual climatological difference between two products (CMv3-CMv4) shows large Q_S values in the Pacific than in other parts of the global tropical oceans.

On the other hand, the annual climatological difference between the two versions of CM downwelling data (Q_L) shows large values of Q_L from CMv4 in the Indian Ocean. Similarly, the annual trend of Q_S and Q_L shows large variability in both versions' tropical oceans. While the northern hemisphere shows a low Q_S annual trend of -0.7 Wm^{-2} , the southern hemisphere shows the annual trend of 1 Wm^{-2} . The large positive annual trend (0.5 Wm^{-2}) in Q_L of CMv3 has been lowered by the CMv4 annual trend over many

parts of the tropical oceans. While annual trends in Q_S are significant at 95%, Q_L shows no such significant trends in both satellite products. The positive annual trends in Q_S may lead to the large annual change in SSTs in the tropical oceans. While positive annual Q_S trends causing southern hemispheric SSTs to increase, negative annual trends show no large impact on the northern hemispheric SSTs.

Similarly, though Q_L annual trends cause SSTs to change in the tropics, these changes are relatively lower than those caused by Q_S and are insignificant. Thus, CMv4 shows significant enhancements in both Q_L and Q_S over the regions of Indo-Pacific warm pool, eastern tropical Pacific, and central Atlantic. However, persisting errors, bias, and low CC values over regions like the tropical Indian Ocean need a relook and demands more study. Similarly, low values of CC over the Indian Ocean highlight the complex nature of cloud patterns and air-sea interactions over the region. As clouds, precipitation, aerosols from forest fires, volcanic eruptions, pollution, and desert storms could greatly affect the downwelling radiation, necessary corrections in the data retrieval techniques from spaceborne instruments could potentially increase the accuracy of the data from space. The impact of coupled climate phenomena like ENSO, MJO, and IOD in tropical oceans plays a vital role in modulating the cloud fraction and precipitation daily to seasonal scales (Zhang 2013). In the future work, we plan to investigate the impact of these events on the variability of downwelling fluxes in the Indian Ocean to understand better the low CC, large bias, and RMSE with in-situ observations over this region. The satellite-derived products underestimate the observed daily variability in terms of standard deviation in all three ocean basins. Though CMv4 has been improved significantly, yet it underestimates the observed values. Hence, this finding may help the data product developer improve it in future releases. Thus, the datasets produced, numerical models run, and climate model outputs validated using the CMv3 need corrections to make their results more accurate. As CMv4 show an apparent enhancement than CMv3, CMv4 could be a better alternative radiation data than the reanalysis or model simulated products for the climate model evaluation and to use as a forcing field to run standalone ocean model.

Declarations

Data Availability Statement

This study utilizes the downwelling radiation data (version 3 and version 4) available from CERES/MODIS program at <https://ceres.larc.nasa.gov/data/#syn1deg-level-3> doi:10.5067/Terra+Aqua/CERES/SYN1deg-3Hour_L3.004A (version 4), doi:10.5067/Terra+NPP/CERES/SYN1deg-3Hour_L3.01A (version 3) and observations from GTMBA moorings available at <https://www.pmel.noaa.gov/gtmba/>, doi:10.5270/OceanObs09.cwp.61. We also used EN4-Hadley interpolated monthly mean temperature profiles available from <https://www.metoffice.gov.uk/hadobs/en4/download-en4-2-1.html>, doi:10.1002/2013JC009067. All data used in the study are available online from the corresponding sources cited in the article and can be found from the above links. However, data supporting this study's findings are available at open access

data repository figshare (Thandlam et al., 2021) and can be accessed through <https://doi.org/10.6084/m9.figshare.15060780.v3>.

Acknowledgements

Authors thank the National Aeronautics and Space Administration (NASA) and the Clouds and the Earth's Radiant Energy System (CERES) program using the Moderate Resolution Imaging Spectroradiometer (MODIS) program for providing downwelling radiation datasets (version 4 doi:10.5067/Terra+Aqua/CERES/SYN1deg-3Hour_L3.004A; version 3 doi:10.5067/Terra+NPP/CERES/SYN1deg-3Hour_L3.01A). Thanks to the GTMBA programme for providing observed downwelling radiation datasets (doi:10.5270/OceanObs09.cwp.61). The authors wish to acknowledge the use of the PyFerret program for analysis and graphics in this paper. PyFerret is a product of NOAA's Pacific Marine Environmental Laboratory (Information is available at <http://ferret.pmel.noaa.gov/Ferret/>). Finally, we acknowledge the Department of Earth Sciences, Uppsala University, and the Swedish Research Council (VR) nr 2017-03988 for supporting this study. Data supporting the study's findings are available at open access data repository figshare and can be accessed through <https://doi.org/10.6084/m9.figshare.15060780.v3>. We are grateful to three anonymous reviewers whose comments/suggestions helped to improve the work and enhance the quality of the article.

Author contributions

V.T. conceived the research plan, performed data analysis, and prepared the first draft, A.R and H.R helped to improve the research plan and M.Y, V.K, and V.R contributed equally to write and review the paper.

Competing interests

The authors declare no competing interests.

References

1. Ali, M. M., Nagamani, P. V., Sharma, N., Venu Gopal, R. T., Rajeevan, M., Goni, G. J., & Bourassa, M. A. (2015). Relationship between ocean mean temperatures and Indian summer monsoon rainfall. *Atmospheric Science Letters*, 16(3), 408–413.
2. Barkstrom, B. R., & Harrison E. F., (1986) First Data From the Earth Radiation Budget Experiment (ERBE), *Bulletin of the American Meteorological Society*, 67(7), 818–824.
3. Barkstrom, B. R., Harrison, E., Smith, G., Green, R., Kibler, J., Cess, R., & the ERBE Science Team, (1989). Earth Radiation Budget Experiment (ERBE) archival and April 1985 results. *Bull. Amer. Meteorol. Soc.*,70:1254–1262.
4. Barkstrom, B., Harrison, E., & Smith, G., (1989) Earth Radiation Budget Experiment (ERBE) Archival and April 1985 Results. *Am. Meteorol. Soc.* 70:1254–1262

5. Bourlès, B., Lumpkin, R., McPhaden, M. J., Hernandez, F., Nobre, P., Campos, E., & Servain, J. (2008). The PIRATA program: history, accomplishments, and future directions. *Bulletin of the American Meteorological Society*, 89(8), 1111–1126.
6. Chowdary JS, Parekh A, Ojha S, Gnanaseelan C (2015) Role of upper Ocean processes in the seasonal SST evolution over tropical Indian Ocean in climate forecasting system. *ClimDyn* 45(9–10):2387–2405
7. Cronin, M.F. and M.J. McPhaden, 1997: The upper ocean heat balance in the western equatorial Pacific warm pool during September-December 1992. *J. Geophys. Res.*, 102, 8533–8553.
8. Curry, J.A., et al (2004) SEAFLUX. *Bull Am Meteorol Soc* 85:409–424
9. De Deckker, P. (2016). The Indo-Pacific Warm Pool: critical to world oceanography and world climate. *Geoscience Letters*, 3(1), 1–12.
10. Doelling, D. R., M. Sun, L. T. Nguyen, M. L. Nordeen, C. O. Haney, D. F. Keyes, P. E. Mlynchak, 2016: Advances in Geostationary-Derived Longwave Fluxes for the CERES Synoptic (SYN1deg) Product, *Journal of Atmospheric and Oceanic Technology*, 33(3), 503–521. doi: 10.1175/JTECH-D-15-0147.1
11. Doelling, D. R., N. G. Loeb, D. F. Keyes, M. L. Nordeen, D. Morstad, C. Nguyen, B. A. Wielicki, D. F. Young, M. Sun, 2013: Geostationary Enhanced Temporal Interpolation for CERES Flux Products, *Journal of Atmospheric and Oceanic Technology*, 30(6), 1072–1090. doi: 10.1175/JTECH-D-12-00136.1
12. Du Y, u T, Meyers G, Masumoto Y, Sasaki H (2005) Seasonal heat budget in the mixed layer of the southeastern tropical Indian Ocean in a high-resolution ocean general circulation model. *J Geophys Res Oceans*. <https://doi.org/10.1029/2004JC002845>
13. Fairall, C.W., Bradley, E.F., Rogers, D.P., Edson, J.B., & Young, G.S., (1996) Bulk parameterization of air-sea fluxes for tropical ocean-global atmosphere coupled ocean-atmosphere response experiment. *J Geophys Res* 101:3747–3764
14. Foltz, G. R., A. T. Evan, H. P. Freitag, S. Brown, and M. J. McPhaden, 2013: Dust accumulation biases in PIRATA shortwave radiation records. *J. Atmos. Ocean. Tech.*, 30, 1414–1432, doi:10.1175/JTECH-D-12-00169.1
15. Foltz, G.R., Evan, A.T., Freitag, H.P., Brown, S., & McPhaden. M.J., (2013) Dust accumulation biases in PIRATA shortwave radiation records. *J Atmos Ocean Technol* 30(7):1414–1432
16. Freitag, H., McCarty, M., & Nosse, C., (1999) COARE Seacat data: Calibrations and quality control procedures.
17. Freitag, H.P., Haleck, M.O., Thomas, G.C., & Mcphaden, M.J., (2001) Calibration procedures and instrumental accuracies for.
18. Good, S. A., M. J. Martin and N. A. Rayner, 2013. EN4: quality controlled ocean temperature and salinity profiles and monthly objective analyses with uncertainty estimates, *Journal of Geophysical Research: Oceans*, 118, 6704–6716, doi:10.1002/2013JC009067
19. Harrison, E., Minnis, F. P., Barkstrom, B. R., Ramanathan, V., Cess, R. D., & Gibson, G. G., (1990) Seasonal variation of cloud radiative forcing derived from the Earth Radiation Budget Experiment. *J.*

- Geophys. Res., 95, 18687–18730.
20. Hartmann, D. L., Moy, L. A., & Fu, Q. (2001). Tropical convection and the energy balance at the top of the atmosphere. *Journal of Climate*, 14(24), 4495–4511.
 21. Hasibur Rahaman, T. Venugopal, Stephen G. Penny, David W. Behringer, M. Ravichandran, J. V. S. Raju, U. Srinivasu & Debasis Sengupta (2019) Improved ocean analysis for the Indian Ocean, *Journal of Operational Oceanography*, 12:1, 16–33, DOI: 10.1080/1755876X.2018.1547261
 22. Hazra A., Chaudhari H.S., Saha Subodh K., Pokhrel S. (2017) Effect of cloud microphysics on Indian summer monsoon precipitating clouds: A coupled climate modeling study, *Journal of Geophysical Research*, 122, March 2017, DOI:10.1002/2016JD026106, 3786–3805.
 23. Hendon HH (2003) Indonesian rainfall variability: impacts of ENSO and local air–sea interaction. *J Clim* 16(11):1775–1790
 24. [https://doi.org/10.1175/1520-0485\(1999\)029%3c1812:TSLHBI%3e2.0.CO;2](https://doi.org/10.1175/1520-0485(1999)029%3c1812:TSLHBI%3e2.0.CO;2)
 25. Jayakumar, A., Vialard, J., & Lengaigne, M., (2011) Processes controlling the surface temperature signature of the Madden–Julian Oscillation in the thermocline ridge of the Indian Ocean. *Clim Dyn* 37:2217–2234. <https://doi.org/10.1007/s00382-010-0953-5>
 26. Kanamitsu, M., Ebisuzaki, W., Woollen, J., Yang, S., Hnilo, J.J., Fiorino, M., & Potter, G.L., (2002) NCEP-DOE AMIP-II reanalysis (R-2). *Bull Am Meteorol Soc* 83:1631–1643.
 27. Kang IS, Jin K, Wang B et al (2002) Intercomparison of the climatological variations of Asian summer monsoon precipitation simulated by 10 GCMs. *Clim Dyn* 19:383–395. <https://doi.org/10.1007/s00382-002-0245-9>.
 28. Kara AB, Rochford PA, Hurlburt HE (2000) An optimal definition for Ocean mixed layer depth. *J Geophys Res Ocean* 105:16803–16821. <https://doi.org/10.1029/2000JC900072>
 29. Kato, S., Loeb, N.G., & Rose, F.G., (2013) Surface irradiances consistent with CERES-derived top-of-atmosphere shortwave and longwave irradiances. *J Clim* 26:2719–2740. <https://doi.org/10.1175/JCLI-D-12-00436.1>
 30. Kobayashi, S., Ota, Y., Harada, Y., Ebata, A., Moriya, M., Onoda, H., ... Takahashi, K. (2015). The JRA-55 reanalysis: General specifications and basic characteristics. *Journal of the Meteorological Society of Japan*. Ser. II, 93(1), 5–48.
 31. Koberle, C., & Philander, S.G.H., (1994) On the processes that control seasonal variations of sea surface temperatures in the tropical Pacific Ocean. *Tellus A* 46:481–496. <https://doi.org/10.1034/j.1600-0870.1994.00011.4>
 32. Koren, I., Feingold, G., and Remer, L. A.: The invigoration of deep convective clouds over the Atlantic: aerosol effect, meteorology or retrieval artifact? *Atmos. Chem. Phys.*, 10, 8855–8872, <https://doi.org/10.5194/acp-10-8855-2010>, 2010.
 33. Lake, B.J., Noor, S.M., Freitag, H.P., & McPhaden, M.J., (2003) Calibration Procedures and Instrumental Accuracy Estimates of ATLAS Air Temperature and Relative.

34. Large, W. G., & Yeager, S. G., (2004) Diurnal to decadal global forcing for ocean and sea-ice models: the data sets and flux climatologies. TN-460 + STR, NCAR, 111 pp. (DOI: 10.5065/D6KK98Q6).
35. Large, W. G., & Yeager, S. G., (2009) The global climatology of an interannually varying air-sea flux data set. *Climate Dynamics*, 33, 341–364 (DOI: 10.1007/s00382-008-0441-3).
36. Li, K. F., Su, H., Mak, S. N., Chang, T. M., Jiang, J. H., Norris, J. R., & Yung, Y. L. (2017). An analysis of high cloud variability: imprints from the El Niño–Southern Oscillation. *Climate Dynamics*, 48(1–2), 447–457.
37. Loeb, N. G., D. R. Doelling, H. Wang, W. Su, C. Nguyen, J. G. Corbett, L. Liang, C. Mitrescu, F. G. Rose, and S. Kato, 2018: Clouds and the Earth’s Radiant Energy System (CERES) Energy Balanced and Filled (EBAF) Top-of-Atmosphere (TOA) Edition-4.0 Data Product. *J. Climate*, 31, 895–918, doi: 10.1175/JCLI-D-17-0208.1.
38. Ma Z, Fei J, Huang X et al (2015) Contributions of surface sensible heat fluxes to tropical cyclone. Part I: evolution of tropical cyclone intensity and structure. *J Atmos Sci* 72:120–140. <https://doi.org/10.1175/JAS-D-14-0199.1>
39. Ma, Y., & Pinker, R.T., (2012) Shortwave radiative fluxes from satellites: an update. *J Geophys Res Atmos*. <https://doi.org/10.1029/2012jd018332>.
40. Mangum, L.J., H.P. Freitag, and M.J. McPhaden (1995): TOGA TAO array sampling schemes and sensor evaluations. Proceedings, Oceans '94 OSATES, 13–16 September 1994, Parc de Penfeld, Brest, France, II-402-II-406.
41. McPhaden, M. & Co-Authors (2010). The Global Tropical Moored Buoy Array in Proceedings of OceanObs'09: Sustained Ocean Observations and Information for Society (Vol. 2), Venice, Italy, 21–25 September 2009, Hall, J., Harrison, D.E. & Stammer, D., Eds., ESA Publication WPP-306, doi:10.5270/OceanObs09.cwp.61.
42. McPhaden, M. J., & Coauthors, (1998). The Tropical Ocean– Global Atmosphere (TOGA) observing system: A decade of progress. *J. Geophys. Res.*, 103, 14 169–14 240, <https://doi.org/10.1029/97JC02906>.
43. Mcphaden, M. J., Meyers, G., Ando, K., Masumoto, Y., Murty, V. S. N., Ravichandran, M., ... Yu, W. (2009). RAMA: The research moored array for African–Asian–Australian monsoon analysis and prediction. *Bulletin of the American Meteorological Society*, 90(4), 459–480.
44. McWilliams, J. C., (1996) Modeling the oceanic general circulation. *Annu. Rev. Fluid Mech.*, 28, 215–248.
45. Medovaya, M., (2002) Assessing ocean buoy shortwave observations using clear-sky model calculations. *J Geophys Res*. doi: 10.1029/2000JC000558.
46. Murtugudde, R. G., Ballabrera-Poy, J., Beauchamp, J., & Busalacchi, A. J. (2001). Relationship between zonal and meridional modes in the tropical Atlantic. *Geophysical research letters*, 28(23), 4463–4466.
47. Payne, R.E., Huang, K., & Weller, R.A., (2002) WHOI-2002-10, A Comparison of Buoy Meteorological Systems.

48. Pinker RT, Bentamy A, Zhang B, Chen W, Ma Y (2017) The net energy budget at the ocean-atmosphere interface of the “Cold Tongue” region. *J Geophys Res Oceans*.
<https://doi.org/10.1002/2016JC012581>
49. Pinker RT, Grodsky SA, Zhang B, Busalacchi A, Chen W (2017) ENSO impact on surface radiative fluxes as observed from space. *J Geophys Res Oceans* 122(10):7880–7896
50. Pinker, R.T., Bentamy, A., Katsaros, K.B., & Ma Y, Li, C., (2014) Estimates of net heat fluxes over the Atlantic Ocean. *J Geophys Res* 119:410–427.
51. Pinker, R.T., Zhang, B.Z., Weller, R.A., & Chen, W., (2018) Evaluating surface radiation fluxes observed from satellites in the southeastern Pacific Ocean. *Geophys Res Lett*.
<https://doi.org/10.1002/2017GL076805>
52. Qiu J (2003) Broadband extinction method to determine aerosol optical depth from accumulated direct solar radiation. *J Appl Meteorol* 42(11):1611–162580.
53. Qu T (2003) Mixed layer heat balance in the western North Pacific. *J Geophys Res Oceans*.
<https://doi.org/10.1029/2002JC001536>.
54. Rahaman, H., & Ravichandran, M., (2013) Evaluation of near-surface air temperature and specific humidity from hybrid global products and their impact on latent heat flux in the North Indian Ocean. *J. Geophys. Res.*, 118, 1034–1047, doi:10.1002/jgrc.20085.
55. Ramanathan, V., Cess, R. D., Harrison, E. F., Minnis, P., Barkstrom, B. R., Ahmad, E., & Hartmann, D., (1989) Cloud-radiative forcing and climate: Results from the Earth Radiation Budget Experiment. *Science*, 243, 57–63
56. Ramesh, M.R.K., Pinker, R.T., Mathew, S., Venkatesan, R., & Chen, W., (2017) Evaluation of radiative fluxes over the north Indian Ocean. *J Theor Climatol*. <https://doi.org/10.1007/s00704-017-2141-6>
57. Riihelä, A., Key, J. R., Meirink, J. F., KuipersMunneke, P., Palo, T., & Karlsson, K. G. (2017). An intercomparison and validation of satellite-based surface radiative energy flux estimates over the Arctic. *Journal of Geophysical Research: Atmospheres*, 122(9), 4829–4848.
58. Rutan, D.A., Kato, S., & Doelling, D.R., (2015) CERES synoptic product: methodology and validation of surface radiant flux. *J Atmos Ocean Technol* 32:1121–1143. <https://doi.org/10.1175/JTECH-D-14-00165.1>
59. Sabeerali, C. T., Ajayamohan, R. S., Bangalath, H. K., & Chen, N. (2019). Atlantic Zonal Mode: An Emerging Source of Indian Summer Monsoon Variability in a Warming World. *Geophysical Research Letters*, 46(8), 4460–4467.
60. Saha, S., et al (2010) The NCEP climate forecast system reanalysis. *Bull m Meteorol Soc* 91:1015–1057
61. Saha, S., et al (2014) The NCEP climate forecast system version 2. *J Clim* 27:2185–2208
62. Smith, G.L., Priestley, K.J., Loeb, & N.G., (2011) Clouds and Earth Radiant Energy System (CERES), a review: Past, present, and future. *Adv Sp Res* 48:254–263. doi: 10.1016/j.asr.2011.03.009

63. Sobel, A.H., Maloney, E.D., Bellon, G., & Frierson, D.M., (2008) The role of surface heat fluxes in tropical intraseasonal oscillations. *Nat Geosci* 1:653–657. <https://doi.org/10.1038/ngeo312>
64. Thandlam, V., & Rahaman, H., (2019). Evaluation of surface shortwave and longwave downwelling radiations over the global tropical oceans. *SN Appl. Sci.* 1, 1171.
65. Thandlam, V., T.V.S, U.B., Hasibur, R. et al. A sea-level monopole in the equatorial Indian Ocean. *npjClim Atmos Sci* 3, 25 (2020). <https://doi.org/10.1038/s41612-020-0127-z>
66. Thandlam, V., T.V.S, U.B., Hasibur, R. et al. A sea-level monopole in the equatorial Indian Ocean. *npjClim Atmos Sci* 3, 25 (2020). <https://doi.org/10.1038/s41612-020-0127-z>
67. Thandlam, Venugopal; Rutgersson, Anna; Rahaman, Hasibur; Yabaku, Mounika; kaagita, venkatramana; Sakirevu Palli, venkatamana reddy (2021): Quantifying Uncertainties in CERES/MODIS Downwelling Radiation Fluxes in the Global Tropical Oceans. figshare. Dataset. <https://doi.org/10.6084/m9.figshare.15060780.v3>
68. Trenberth, K.E., and David, P., & Stepaniak., (2004). The Flow of Energy Through the Earth's Climate System. *Quarterly Journal of the Royal Meteorological Society* 130 (603): 2677–2701.
69. Trolliet, M., Walawender, J. P., Boulès, B., Boilley, A., Trentmann, J., Blanc, P., Lefèvre, M., and Wald, L.: Downwelling surface solar irradiance in the tropical Atlantic Ocean: a comparison of re-analyses and satellite-derived data sets to PIRATA measurements, *Ocean Sci.*, 14, 1021–1056, <https://doi.org/10.5194/os-14-1021-2018>, 2018.
70. Venugopal, T., Ali, M.M., Bourassa, M.A. et al. Statistical Evidence for the Role of Southwestern Indian Ocean Heat Content in the Indian Summer Monsoon Rainfall. *Sci Rep* 8, 12092 (2018). <https://doi.org/10.1038/s41598-018-30552-0>
71. Venugopal, T., Rahaman, H., Ravichandran, M., & Ramakrishna, S. S. V. S., (2016). Evaluation of MODIS/CERES downwelling shortwave and longwave radiation over global tropical oceans, *Proc. SPIE* 9876, *Remote Sensing of the Atmosphere, Clouds, and Precipitation VI*, 98761F; <https://doi.org/10.1117/12.2228041>
72. Vialard J, Menkes C, Boulanger JP, Delecluse P, Guilyardi E, McPhaden MJ, Madec G (2001) A model study of Oceanic mechanisms affecting equatorial Pacific sea surface temperature during the 1997–98 El Niño. *J Phys Oceanogr* 31(7):1649–1675
73. Vialard, J., Foltz, G.R., & McPhaden, M.J., (2008) Strong Indian Ocean sea surface temperature signals associated with the Madden-Julian Oscillation in late 2007 and early 2008. *Geophys Res Lett* 35:L19608. <https://doi.org/10.1029/2008GL035238>
74. Vimont DJ, Kossin JP (2007) The Atlantic Meridional Mode and hurricane activity. *Geophys Res Lett* 34:L07709. <https://doi.org/10.1029/2007GL029683>
75. Wang W, McPhaden MJ, Wang W, McPhaden MJ (1999) The surface-layer heat balance in the equatorial Pacific Ocean. Part I: mean seasonal cycle*. *J Phys Oceanogr* 29:1812–1831.
76. Wang, H., & Mehta, V. M. (2008). Decadal variability of the Indo-Pacific warm pool and its association with atmospheric and oceanic variability in the NCEP–NCAR and SODA reanalyses. *Journal of Climate*, 21(21), 5545–5565.

77. Wang, H., & Pinker, R. T., (2009) Shortwave radiative fluxes from MODIS: Model development and implementation. *J. Geophys. Res.*, 114, D20201, doi:10.1029/2008JD010442.
78. Weller, R.A., J.T. Farrar, J. Buckley, S. Mathew, R. Venkatesan, J. SreeLekha, D. Chaudhuri, N. Suresh Kumar, and B. Praveen Kumar. 2016. Air-sea interaction in the Bay of Bengal. *Oceanography* 29(2):28–37, <http://dx.doi.org/10.5670/oceanog.2016.36>.
79. Wielicki, B. A., Barkstrom, B. R., Harrison, E. F., Lee, R. B. III, & Smith, L., (1996). Clouds and the Earth's radiant energy system (CERES): an Earth observing system experiment. *Bull. Amer. Meteor. Soc.* 77, 853–868.
80. Wielicki, B.A., Barkstrom, B.R., & Baum, B.A., (1998) Clouds and the earth's radiant energy system (CERES): algorithm overview. *IEEE Trans Geosci Remote Sens* 36:1127–1141. <https://doi.org/10.1109/36.701020>.
81. Woollings, T., Gregory, J. M., Pinto, J. G., Reyers, M., & Brayshaw, D. J. (2012). The response of the North Atlantic storm track to climate change shaped by ocean-atmosphere coupling. *Nature Geoscience*, 5(5), 313–317.
82. Xie S-P, Philander SGH (1994) A coupled Ocean-atmosphere model of relevance to the ITCZ in the eastern Pacific. *Tellus A* 46:340–350. <https://doi.org/10.1034/j.1600-0870.1994.t01-1-00001.x>
83. Xie, S. P., & Carton, J. A. (2004). Tropical Atlantic variability: Patterns, mechanisms, and impacts. *Earth's Climate: The Ocean-Atmosphere Interaction*, *Geophys. Monogr*, 147, 121–142.
84. Zhang, C. (2013). Madden–Julian oscillation: Bridging weather and climate. *Bulletin of the American Meteorological Society*, 94(12), 1849–1870.
85. Zhang, Y.C., Rossow, W.B., Lacis, A.A., Oinas, V., & Mishchenko, M.I., (2004) Calculation of radiative fluxes from the surface to top of atmosphere based on ISCCP and other global data sets: Refinements of the radiative transfer model and the input data. *J. Geophys. Res.*, 109, D19105, doi:10.1029/2003JD004457

Tables

Table 1: Details of GTMBA data used to evaluate CM data during 2000-2015

Region/Parameter	Q _S		Q _L		Temporal resolution	Reference
	No. of stations	No. of daily observations	No. of stations	No. of daily observations		
Indian Ocean/RAMA	19	42412	3	8188	daily	McPhaden et al. (2009)
Atlantic Ocean/PIRATA	17	68537	4	13872	daily	Bourlès et al. (2008)
Pacific Ocean/TIO/TRITON	32	90654	11	14294	daily	McPhaden et al. (1998)

Table 2: Statistics of Q_S and Q_L from CMv3 and CMv4 compared with RAMA in the Indian Ocean using daily data during 2000-2015.

Parameter	Q_S (RAMA Mean =225.6 Wm^{-2} , RAMA STD=68.72 Wm^{-2}) No. of RAMA observations=42412		Q_L (RAMA Mean=414.1 Wm^{-2} , RAMA STD=26.78 Wm^{-2}) No. of RAMA observations=8188	
	CMv3	CMv4	CMv3	CMv4
Bias (Wm^{-2})	4.54	1.43	-6.95	-3.15
STD (Wm^{-2})	52.43	58.49	21.73	21.05
RMSE (Wm^{-2})	41.33	27.34	14.91	12.96
Mean (Wm^{-2})	230.1	227	407.1	410.9
CC (Wm^{-2})	0.80	0.92	0.87	0.89

Table 3: Statistics of Q_S and Q_L from CMv3 and CMv4 compared with PIRATA in the Atlantic Ocean using daily data during 2000-2015.

Parameter	Q_S (PIRATA Mean=230.52 Wm^{-2} , PIRATA STD=56.81 Wm^{-2}) No. of PIRATA observations=68537		Q_L (PIRATA Mean=404.4 Wm^{-2} , PIRATA STD=15.9 Wm^{-2}) No. of PIRATA observations=13872	
	CMv3	CMv4	CMv3	CMv4
Bias (Wm^{-2})	7.36	4.39	-4.84	3.57
STD (Wm^{-2})	42.65	49.67	15.58	16.26
RMSE (Wm^{-2})	35.84	26.18	10.39	7.11
Mean (Wm^{-2})	237.9	234.9	399.6	403.2
CC (Correlation Coefficient) (Wm^{-2})	0.79	0.89	0.82	0.82

Table 4: Statistics of Q_S and Q_L from CMv3 and CMv4 compared with TAO/TRITON in the Pacific Ocean using daily data during 2000-2015.

Parameter	Q_S (TRITON Mean=227.5 Wm^{-2} , TRITON STD=65.11 Wm^{-2}) No. of TRITON observations=90654		Q_L (TRITON Mean=408.13 Wm^{-2} , TRITON STD=18.12 Wm^{-2}) No. of TRITON observations=14294	
	CMv3	CMv4	CMv3	CMv4
Bias (Wm^{-2})	7.34	-0.67	-3.26	4.96
STD (Wm^{-2})	47.07	53.99	14.47	15.94
RMSE (Wm^{-2})	40.92	28.91	9.73	7.56
Mean (Wm^{-2})	234.8	226.9	404.9	409.8
CC (Wm^{-2})	0.79	0.90	0.87	0.91

Table 5: Annual trend in the GTMBA data over selected locations in the global tropical oceans. Empty cells correspond to unavailability of sufficient no. of observations.

Indian Ocean			
s.no	station location	Q_S trend ($Wm^{-2}/Year$)	Q_L trend ($Wm^{-2}/Year$)
1	0N80.5E	-0.41	-0.56
2	0N90E	-1.47	-
3	15N90E	-2.72	1.58
4	1.5S90E	1.40	-
5	8S67E	0.53	-
Atlantic Ocean			
6	0N23W	0.25	-0.10
7	10S10W	-0.31	-0.33
8	12N23W	-1.32	1.20
9	15N38W	-0.10	0.54
10	6S10W	-0.31	-
Pacific Ocean			
11	0N110W	-0.16	1.4
12	0N140W	1.0	1.58
13	0N165E	0.31	0.01
14	0N170W	-0.87	0.67

Figures

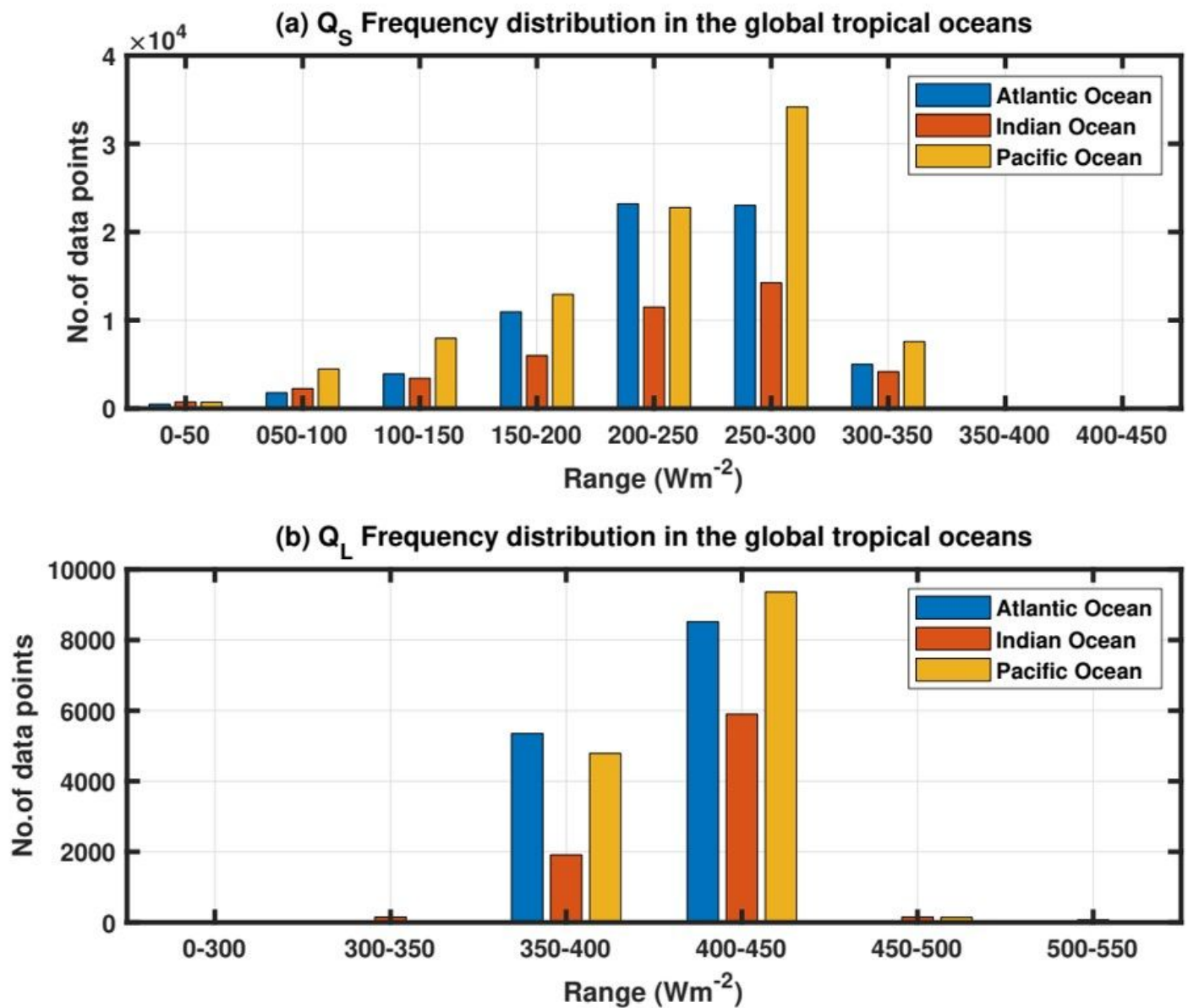


Figure 1

Frequency distribution of (a) Q_S (Wm^{-2}) and (b) Q_L (Wm^{-2}) in tropical oceans using daily data during 2000-2015.

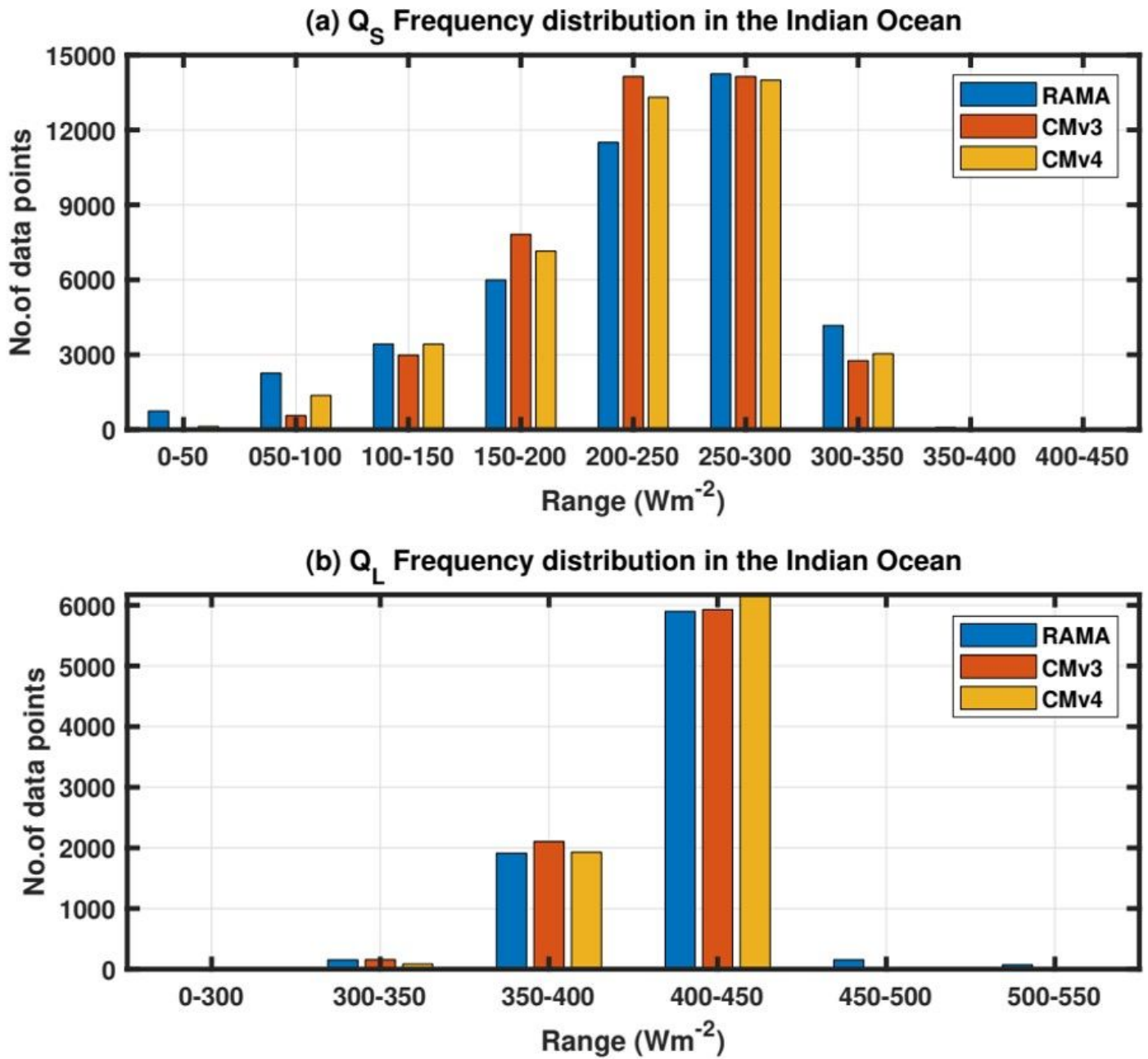


Figure 2

Frequency distribution of (a) Q_S and (b) Q_L in the Indian Ocean from RAMA and CM using daily data during 2000-2015.

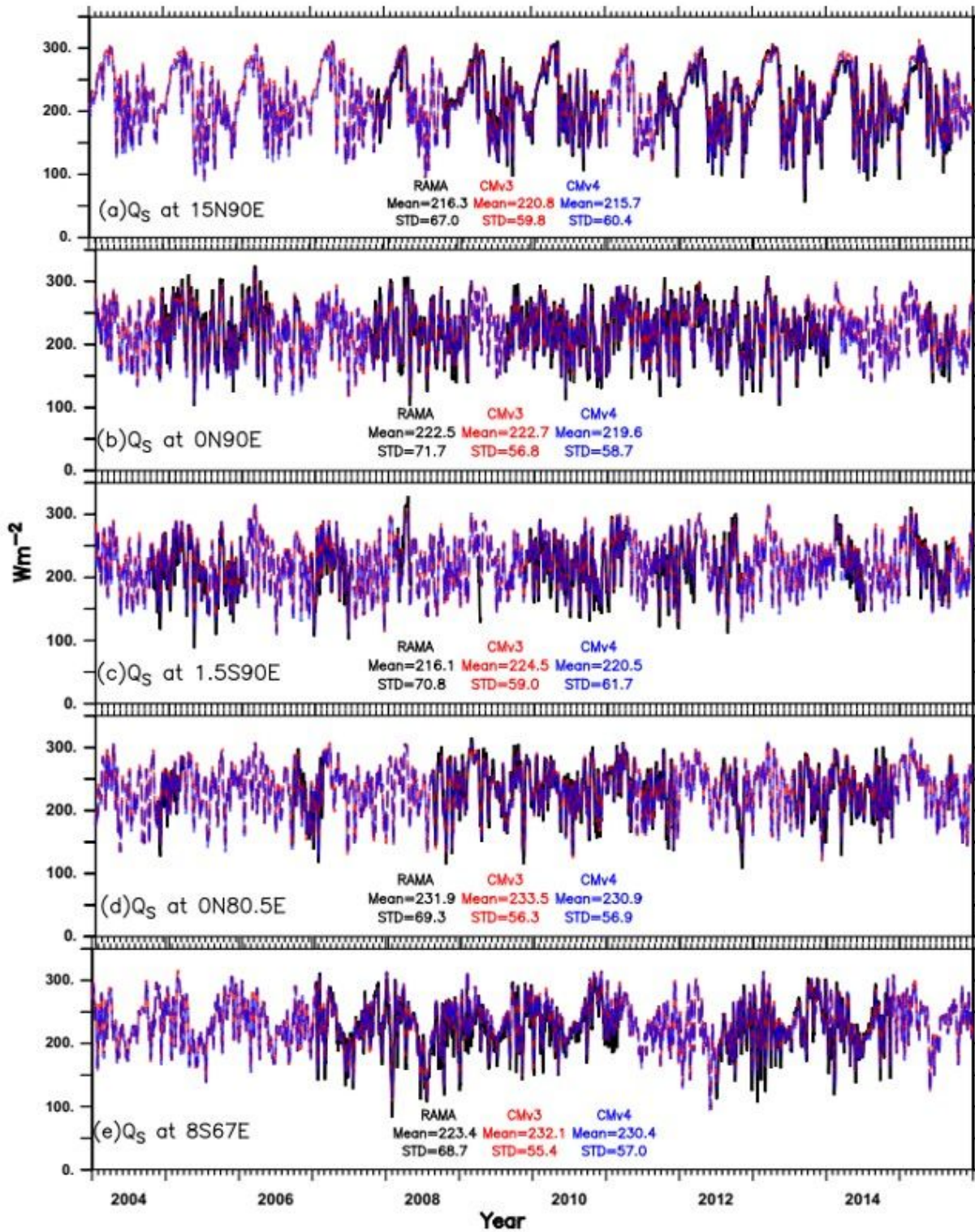


Figure 3

Temporal variability of Q_S from CMv3 (red) and CMv4 (blue) compared with RAMA (black) in the Indian Ocean during 2000-2015. Data plotted using 7-day running mean (smoothing). Discontinuous black lines are due to unavailability of observations during those time steps.

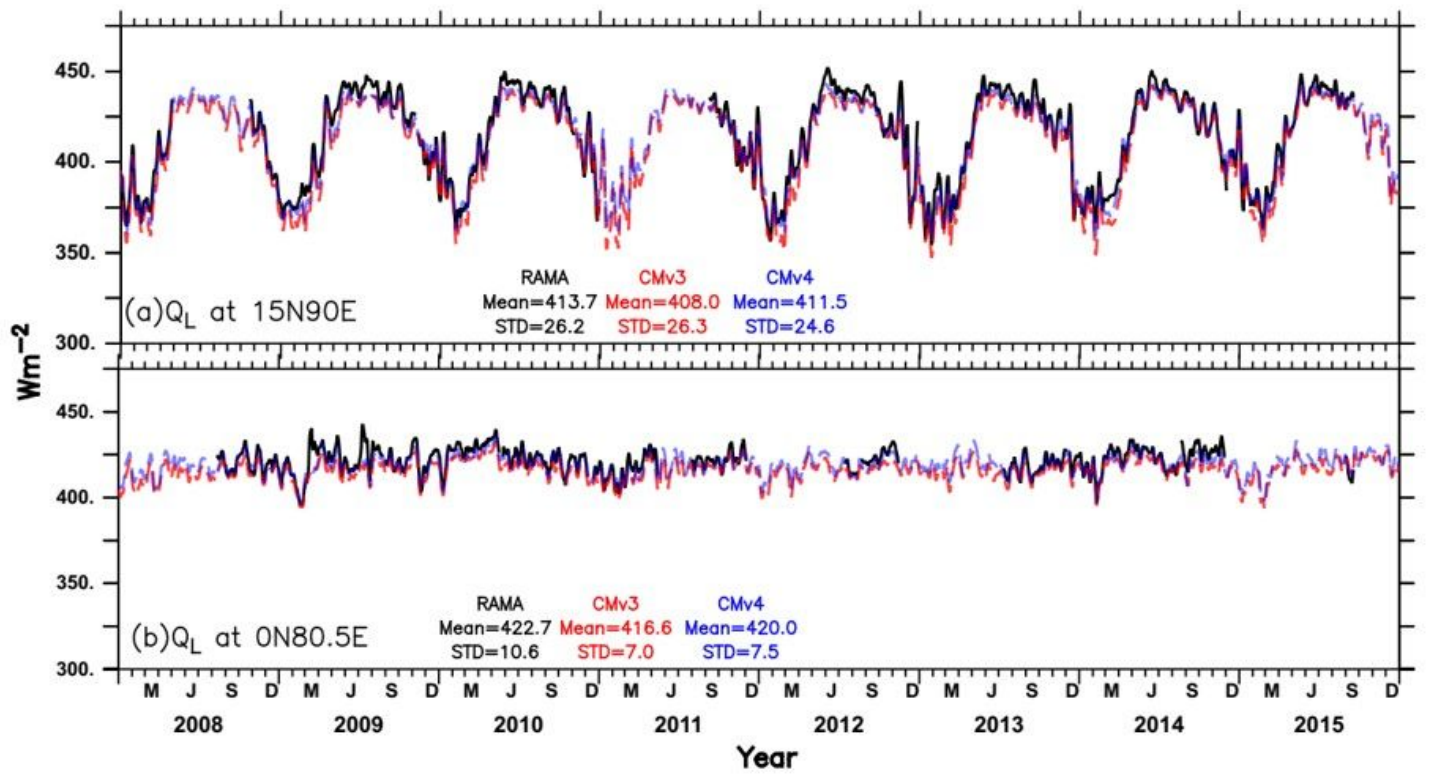


Figure 4

Temporal variability of Q_L in CMv3 (red) and CMv4 (blue) compared with RAMA (black) in the Indian Ocean during 2000-2015. Data plotted using 7-day running mean (smoothing). Discontinues black lines are due to unavailability of observations during those time steps.

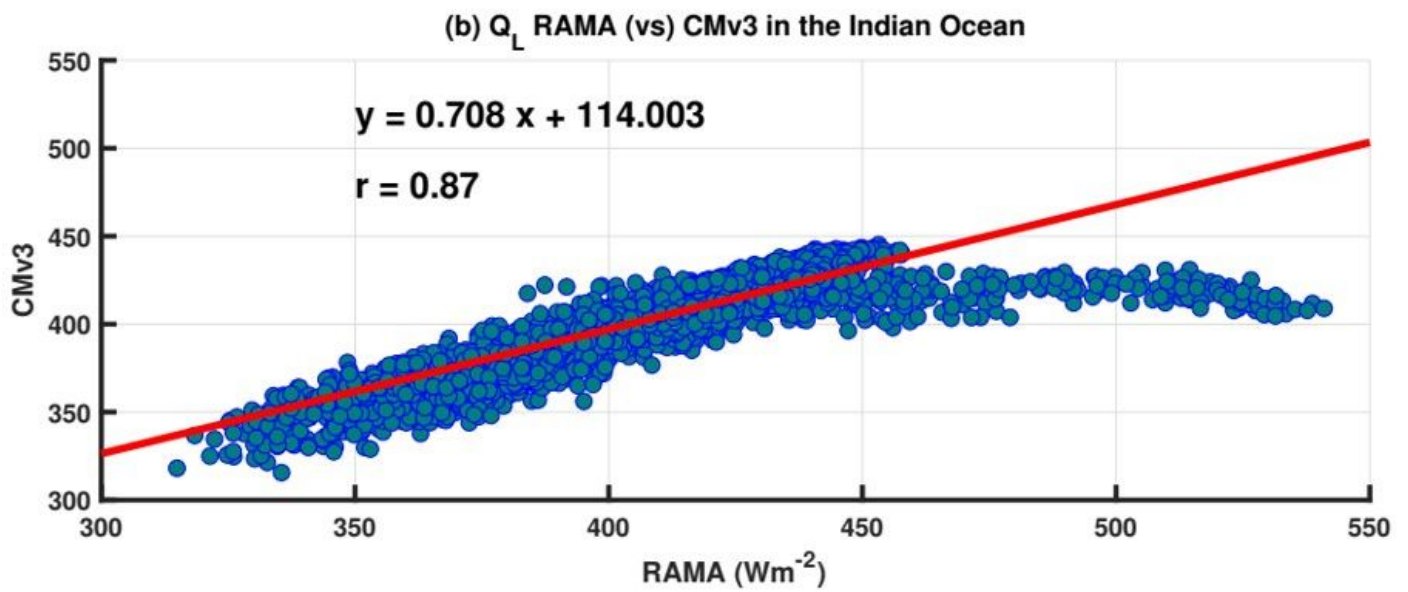
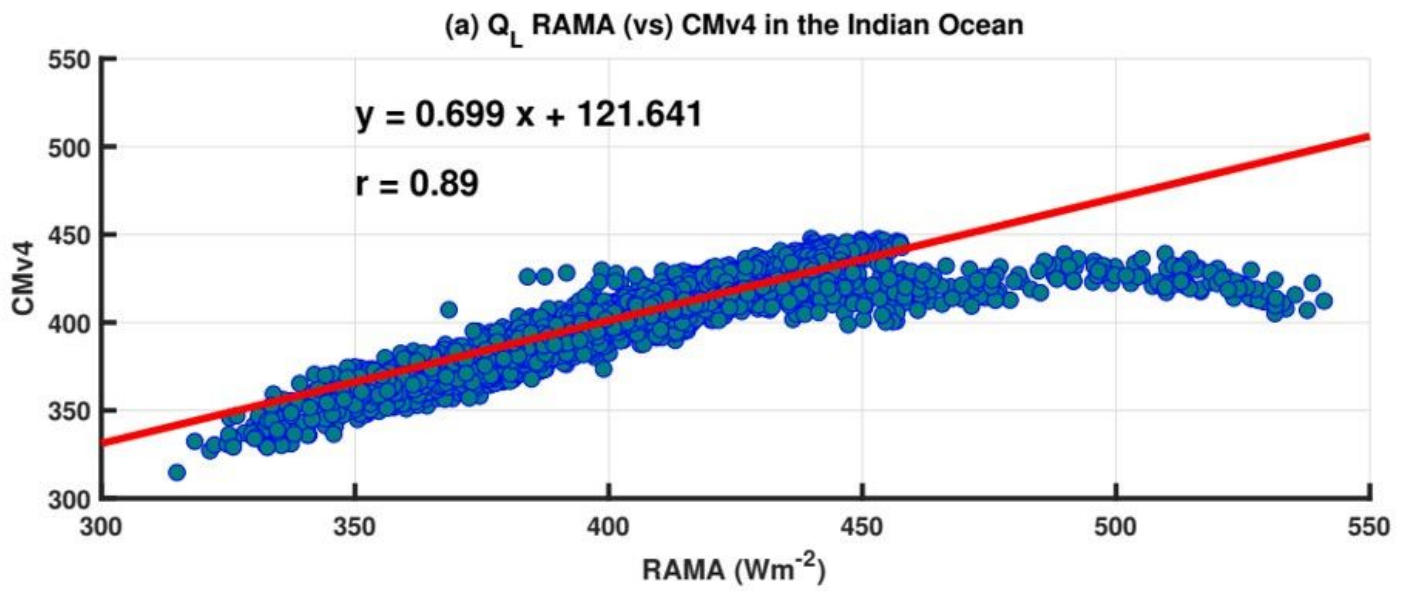


Figure 5

Scatter plots showing Q_L from (a) CMv4 and (b) CMv3 compared with observations (RAMA) in the Indian Ocean using daily data during 2000-2015.

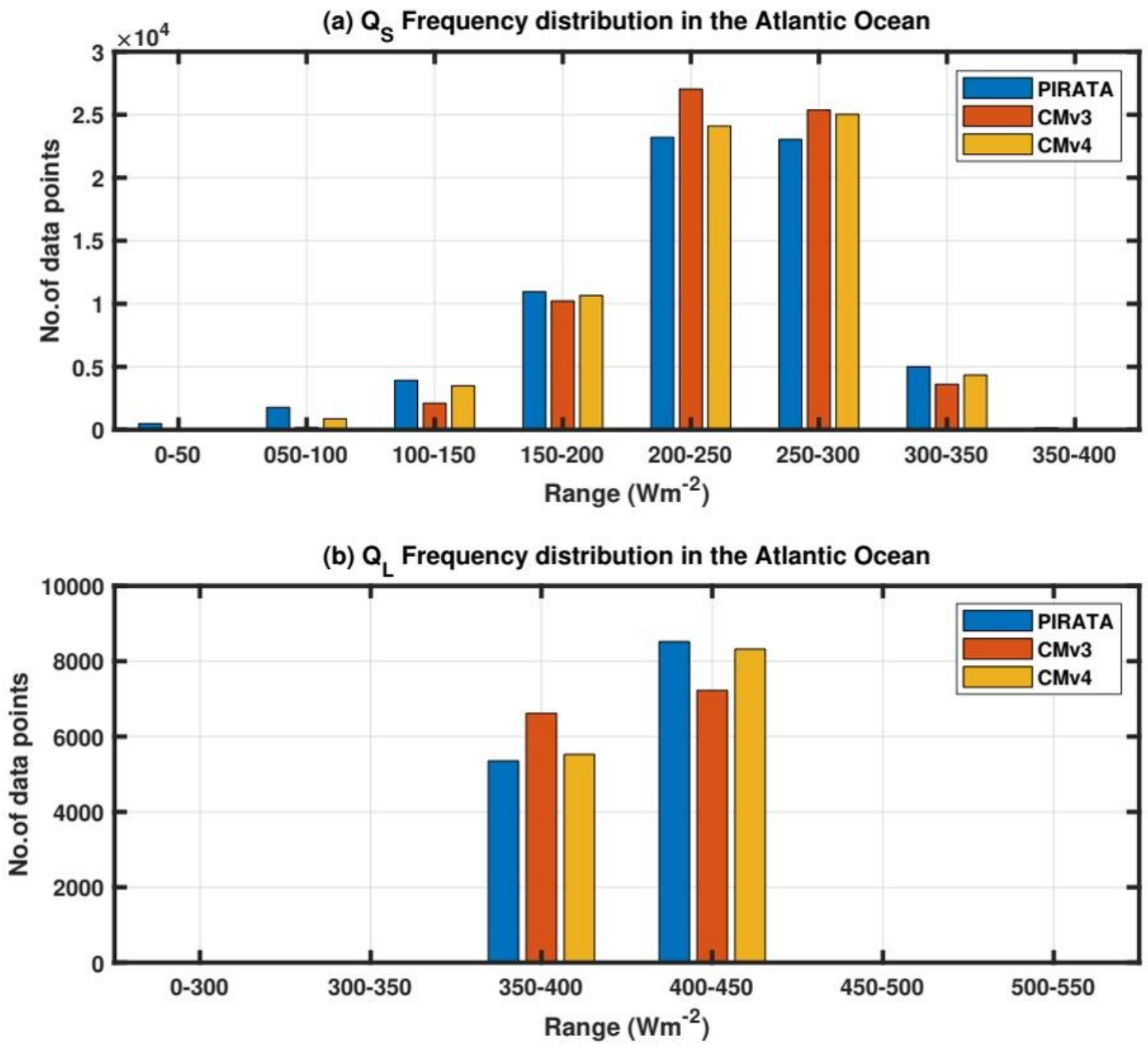


Figure 6

Frequency distribution of (a) Q_S and (b) Q_L in the tropical Atlantic Ocean from PIRATA and CM using daily data during 2000-2015.

Figure 7

Temporal variability of Q_S from CMv3 (red) and CMv4 (blue) compared with PIRATA (black) in the tropical Atlantic Ocean during 2000-2015. Data plotted using 7-day running mean (smoothing). Discontinues black lines are due to unavailability of observations during those time steps.

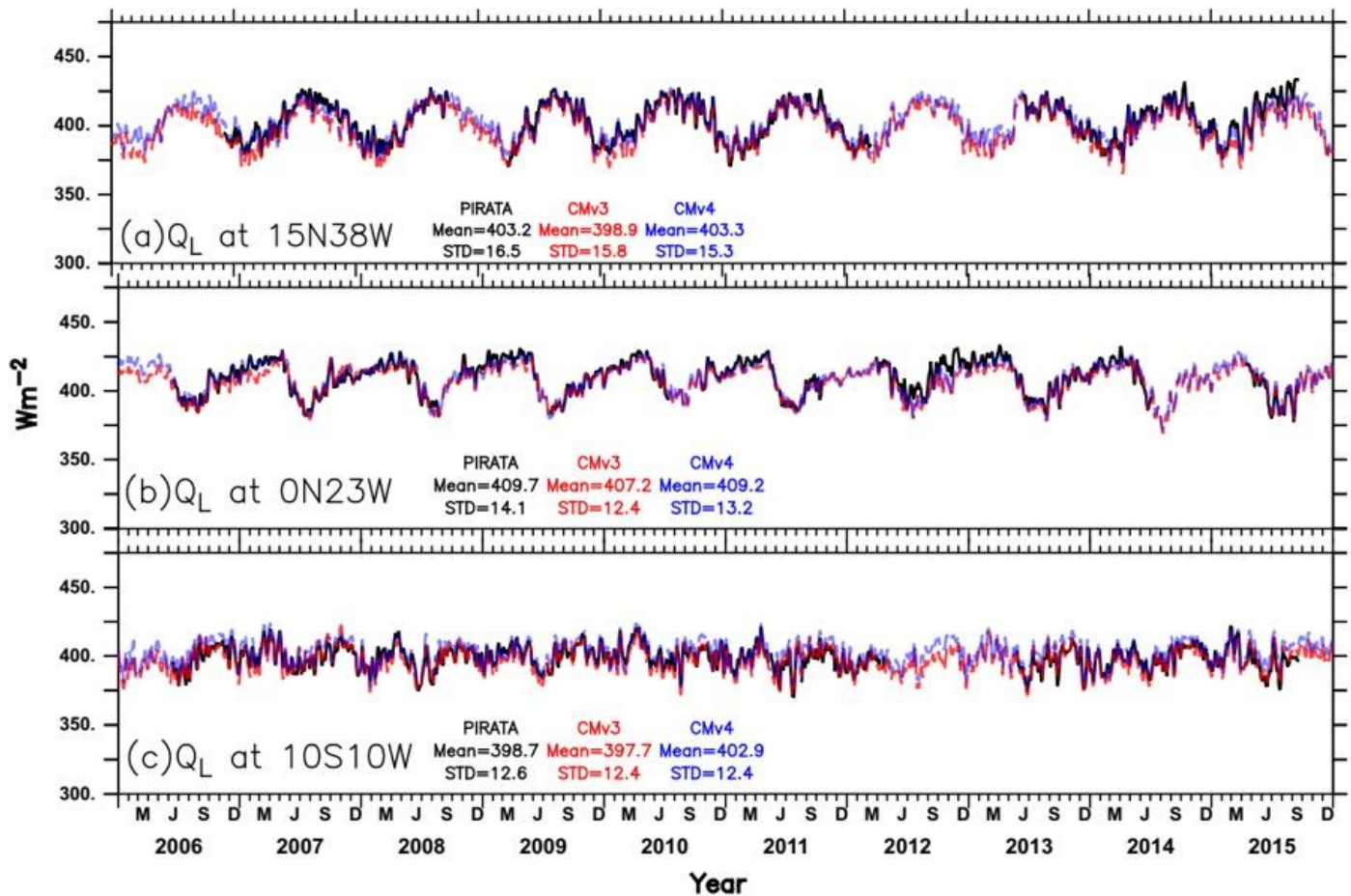


Figure 8

Temporal variability of Q_L from CMv3 (red) and CMv4 (blue) compared with PIRATA (black) in the tropical Atlantic Ocean during 2000-2015. Data plotted using 7-day running mean (smoothing). Discontinues black lines are due to unavailability of observations during those time steps.

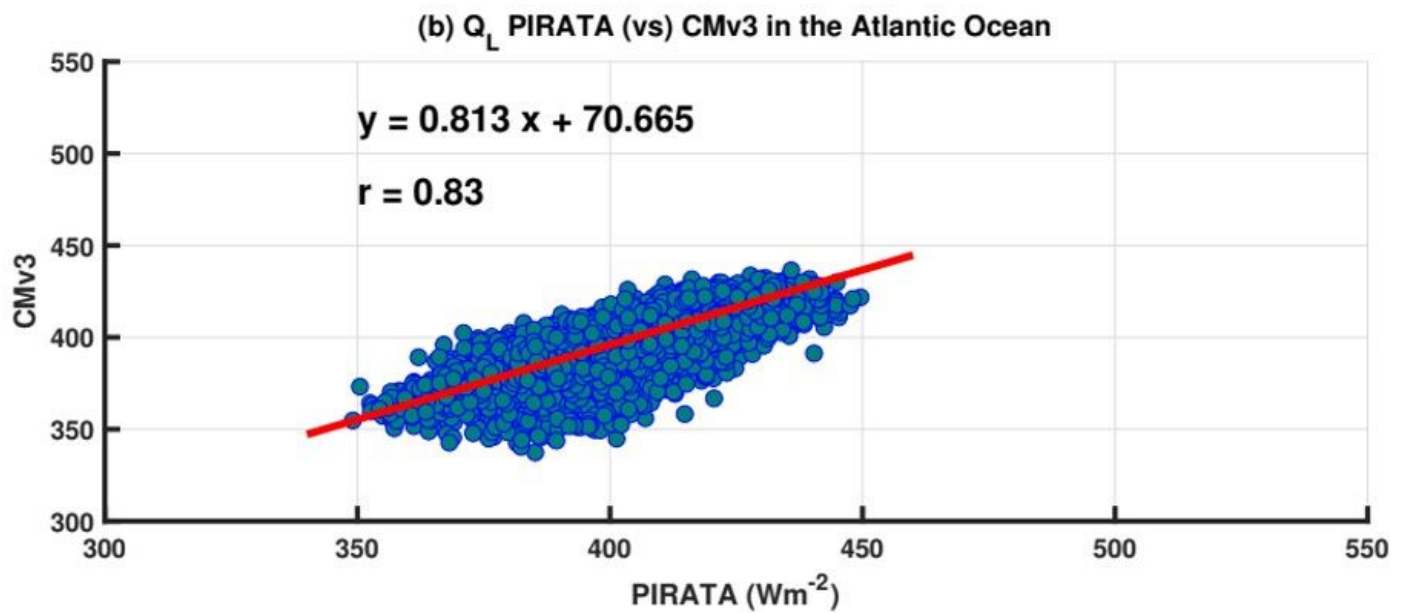
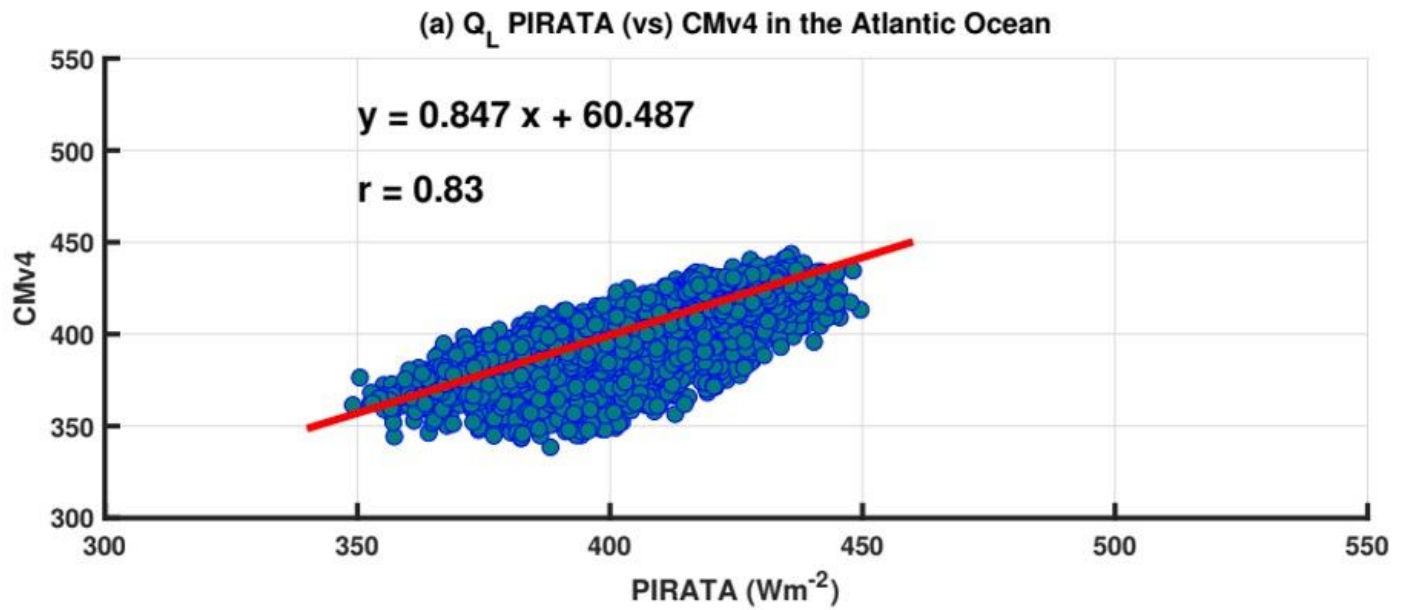


Figure 9

Scatter plots showing Q_L from (a) CMv4 and (b) CMv3 compared with observations (PIRATA) in the tropical Atlantic Ocean using daily data during 2000-2015.

Figure 10

Frequency distribution of (a) Q_S and (b) Q_L in the tropical Pacific Ocean from TAO/TRITON and CM using daily data during 2000-2015.

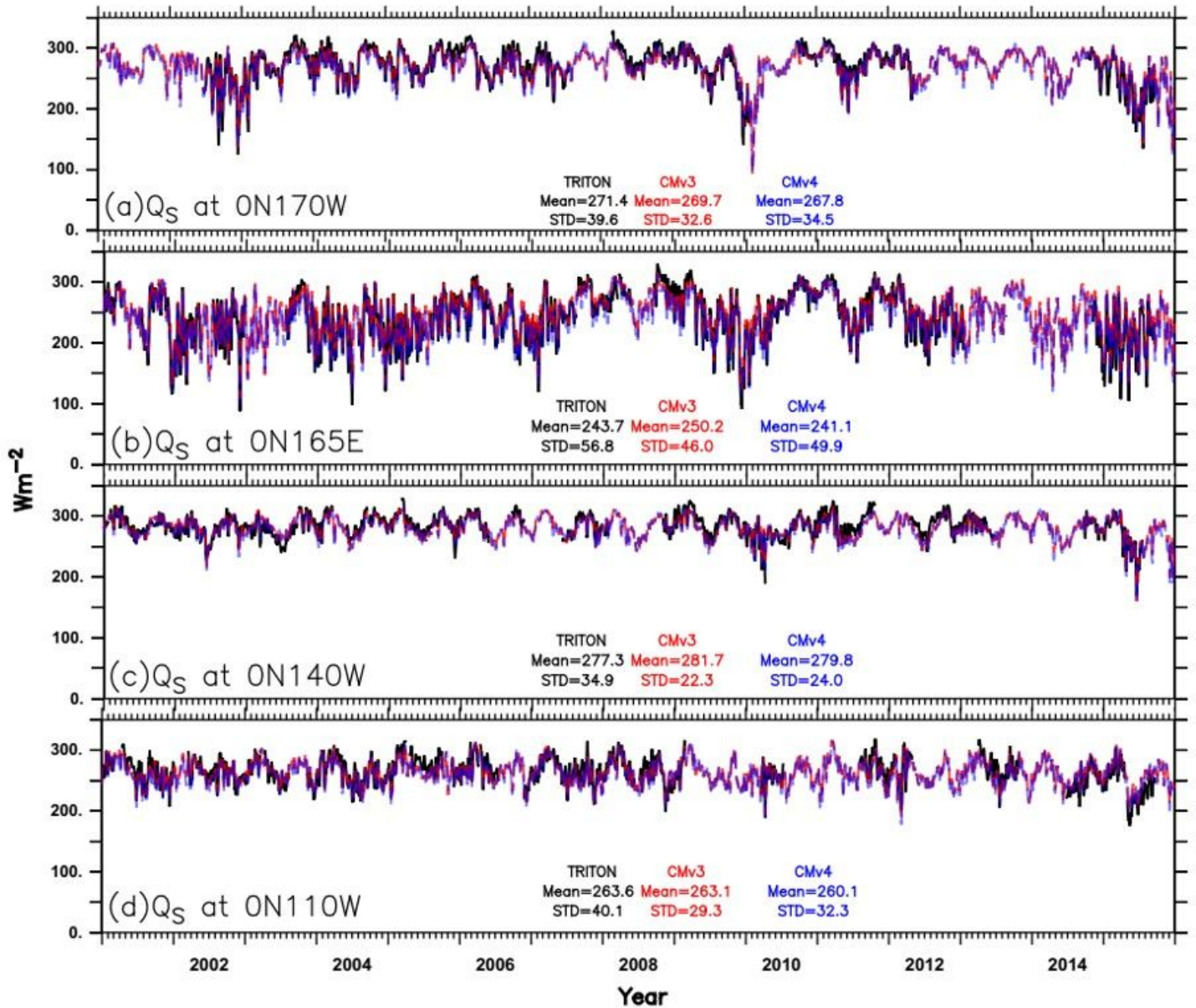


Figure 11

Temporal variability of Q_S (Wm^{-2}) from CMv3 (red) and CMv4 (blue) compared with TAO/TRITON (black) in the tropical Pacific Ocean during 2000-2015. Data plotted using 7-day running mean (smoothing). Discontinuities black lines are due to unavailability of observations during those time steps.

Figure 12

Temporal variability of Q_L from CMv3 (red) and CMv4 (blue) compared with TAO/TRITON (black) in the tropical Pacific Ocean during 2000-2015. Data plotted using 7-day running mean (smoothing).

Discontinues black lines are due to unavailability of observations during those time steps.

Figure 13

Scatter plots showing Q_L from (a) CMv4 and (b) CMv3 compared with observations (TAO/TRITON) in the tropical Pacific Ocean during 2000-2015.

Figure 14

Seasonal mean of Q_S from CMv3 and CMv4 in the global tropical oceans during Mar 2000- Feb 2017.

Figure 15

Seasonal mean of Q_L from CMv3 and CMv4 in the global tropical oceans during Mar 2000- Feb 2017.

Figure 16

Climatology of Q_S (a and b) and Q_L (c and d) from CMv3 and CMv4, respectively, in the global tropical oceans during Mar 2000- Feb 2017.

Figure 17

Difference in climatology of (a) Q_S and (b) Q_L between CMv3 and CMv4 in the global tropical oceans during Mar 2000- Feb 2017.

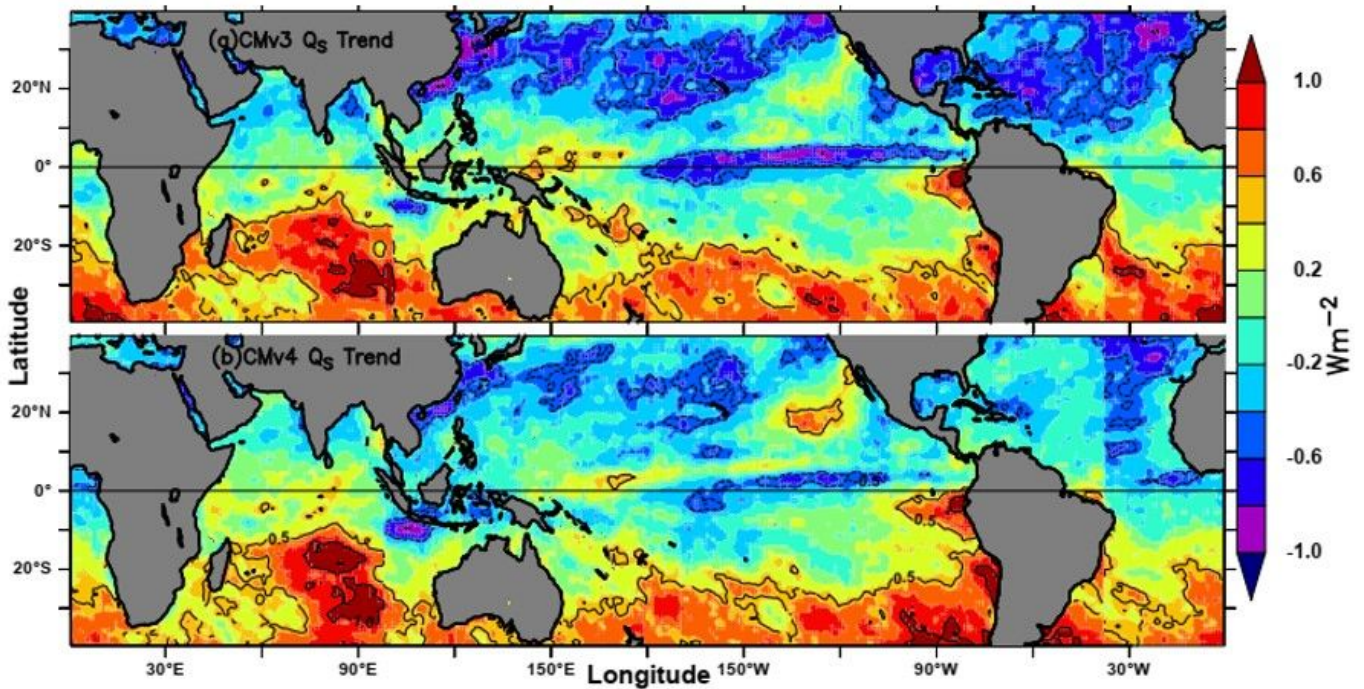


Figure 18

Annual trend of Q_s in (a) CMv3 and (b) CMv4 in the global tropical oceans during Mar 2000- Feb 2017. Contours with continuous and dashed lines show the significant (95%) positive and negative trends, respectively.

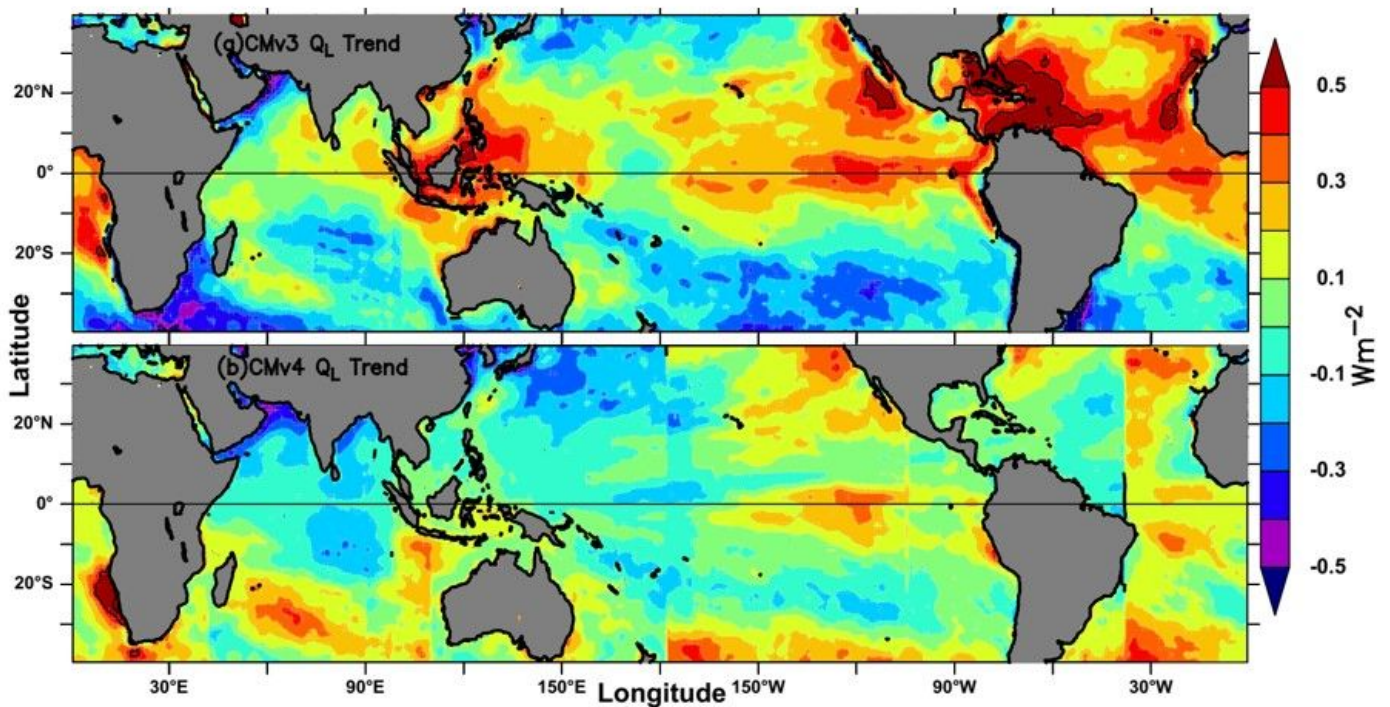


Figure 19

Annual trend of Q_L in (a) CMv3 and (b) CMv4 in the global tropical oceans during Mar 2000- Feb 2017. Contours with continuous and dashed lines show the significant (95%) positive and negative trends, respectively.

Figure 20

Annual change in SST due to annual trend in (a) Q_S and (b) Q_L from CMv4 in the global tropical oceans during 2000-2017.

Supplementary Files

This is a list of supplementary files associated with this preprint. Click to download.

- [Supplementarymaterial.docx](#)